# Study of Hyperfine Structure of Some Iron Compounds Using Mössbauer Effect

by

Wen-Hwei Tsau

A thesis submitted in partial fulfillment of the requirement for the degree of Master of Science.

Department of Physics
Sir George Williams University
Montreal

September 1, 1969

ACKNOWLEDGEMENTS

The author wishes to thank Dr. R. C. Sharma for his guidance, assistance and encouragement throughtout this work.

Special thanks are due to :
Department of Physics, Sir George Williams University for laboratory and workshop facilities;
Mr. J. Blaison for the help of setting up the equipment;
and Mr. Vo Van Thanh for useful discussion.

CONTENTS

# ABSTRACT

The compounds used in this investigation are powder crystal of ferric oxide ($Fe_2O_3$) and some other hydrate iron compounds, such as: ferrous sulfate ($FeSO_4 \cdot 7H_2O$), ferrous chloride ($FeCl_2 \cdot 4H_2O$), ferric sulfate ($Fe_2(SO_4)_3 \cdot 9H_2O$), ferric chloride ($FeCl_3 \cdot 6H_2O$), ferric nitrate ($Fe(NO_3)_3 \cdot 9H_2O$), potasium ferrocyanide ($K_4Fe(CN)_6 \cdot 3H_2O$) and sodium nitroprusside ($Na_2Fe(CN)_5NO \cdot 2H_2O$).

The hyperfine interaction between the nucleus and its surrounding are expressed in terms of electromagnetic moments. Calibration curve modified to suit the measurements in this work, is used to obtain the percentage of 4s-electron contribution in iron compounds. Using these values, the electronic charge densities at nucleus are calculated by Roothaan-Hartree-Fock method, which are found to be slightly higher than the values calculated directly from the experimental results. The electric field gradient in the compounds is calculated from the measurements of quadrupole splitting. The quadrupole splitting is also calculated for divalent compounds. The internal magnetic field of ferric oxide is estimated from the magnetic hyperfine splitting and the results are in good agreement with those of Kistner and Sunyar.

# INTRODUCTION

The resonant absorption phenomena have been known in optics since early in the century. The nuclear analogue was predicted in 1929 (ref. 1) and was observed in 1951 (ref. 2). The phenomenon of recoilless nuclear resonance was discovered by R. L. Mössbauer in 1958 (ref. 3) and recognized by the award of Nobel Prize in 1961. Since then, it has drawn the attention of scientists for the last decade. This discovery makes it possible to observe the narrow gamma lines which can be used in many fields because of the high energy resolution.

Mössbauer Effect was soon recognized as a technique for the study of the wide range of the phenomena. In this work, a study of hyperfine structure of chemical compounds is made from the measurements of nuclear isomer shift, quadrupole splitting and magnetic hyperfine splitting using Mössbauer spectroscopy. From the observed value of isomer shift, the charge densities at nucleus are calculated. The theoretical calculation of the charge densities are also done by Roothaan-Hartree-Fock method, and a comparison is made with the empirical values. The electric field gradients in iron compounds are calculated from observed quadrupole splitting. The quadrupole splitting is calculated for divalent compounds by considering the electric field due to d-orbitals. An estimate of the internal magnetic field in iron oxide is made from the measure-

ment of magnetic hyperfine splitting. In this work, a serious attempt has been made to study these hyperfine interactions in various iron compounds and to gather information from the observed Mössbauer Effect spectra.

Chapter I in this work contains the general theory of Mössbauer Effect, a description of the equipment and its use in the study of Mössbauer Effect. Chapter II gives the effect of hyperfine interactions between the nucleus and its surroundings. The interactions are derived in terms of electromagnetic moments. The general applications of $Fe^{57}$ and included in Chapter III. The experimental procedure are the results are discussed in Chapter IV. The theoretical derivation of various expression relating to hyperfine interactions and other numerical works are included in appendices.

# Chapter I

## Mössbauer Effect Spectrometer

A. The Mössbauer Effect

It is a well-known fact that the emission of gamma rays by nuclei takes place as a result of transition between energy levels of the nuclei. As the gamma photon carries away most of momentum, a small part of recoil momentum is imparted to the de-excited nucleus. The recoil energy $E_R$ of the residual nucleus is $E_R = E^2/2Mc^2$, E being the energy of emitted gamma ray, M being the mass of nucleus and c being the velocity of light. The energy difference, $\delta E = E_o - E$, between the transition energy $E_o$ and that of gamma ray energy E actually carried by gamma ray, consists of two parts: (1) the free-atom recoil energy $E_R$, which is independent of initial velocity of the nucleus and (2) a term arising due to the well-known Doppler effect, which is linear in velocity of the atom if it is moving.

The fraction of energy $E_R$, which is lost to the recoiling atom is small. For example, in case of gamma rays of energy 100 keV and a nucleus of mass number 100, the recoil energy is only 5 parts in $10^7$. Before Mössbauer's discovery, it was impossible to detect small energy difference of this order. However, this small energy loss becomes significant when it is compared with the natural line width of gamma rays. This finite line width arises from the finite time which the nucleus spends in an excited state, The line width $\Gamma$ and life time $\tau$ of the nuclear state are related by

$$\Gamma\tau = \hbar$$

or

$$\Gamma = (0.693/\tau_{\frac{1}{2}})\ \hbar$$

According to this relation, a typical lifetime of $\tau_{\frac{1}{2}} = 10^{-7}$sec. will result in a line width of $4.6 \times 10^{-9}$eV, which is very much smaller than the energy ($E_R \approx 5 \times 10^{-7}$) lost in nuclear recoil. Therefore, the gamma-ray emission line of energy $E_o - E_R$ does not overlap the absorption line of energy $E_o + E_R$ when $\Gamma < E_R$, and the nuclear resonance absorption is not observable as explained in the Fig. 1-1.

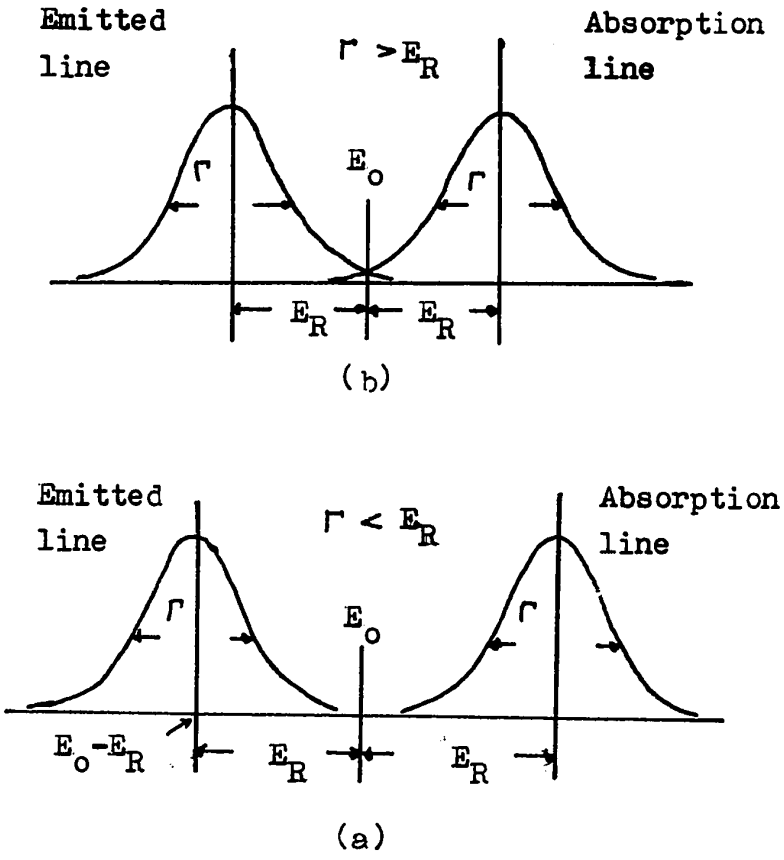


Fig. 1-1 (a) Resonant absorption is not possible if the recoil energy loss exceeds the linewidth. (b) Emitted gamma line overlaps the absorption line and partial resonance takes place.

P. B. Moon (ref. 4) was able to bring the emission and absorption lines back into coincidence by compensating for the recoil energy loss by using the principle of Doppler shift. According to Doppler shift, the energy of radiation emitted by a source moving towards an absorber with velocity V is increased by an amount EV/c. By placing the radioactive source on a rapidly spinning wheel, Moon was able to bring about resonant scattering.

Another method to compensate for the recoil loss makes use of the thermal motion of the atom in a gas. The gas atoms have a Maxwellian velocity distribution which in effect broadens the emission and absorption lines. This causes resonant scattering when the broadened lines begin to overlap.

While comparing the scattering of the 129 keV gamma rays of $Ir^{191}$ by Ir and Pt, Mössbauer (ref. 3) found an increase in scattering in Ir at low temperature, which was contrary to classical predictions. The interpretation of this effect was first given by Mössbauer and is therefore called after his name.

A basic setup to study the recoil free emission and absorption of gamma rays using Mössbauer Effect is given in Fig. I-2.

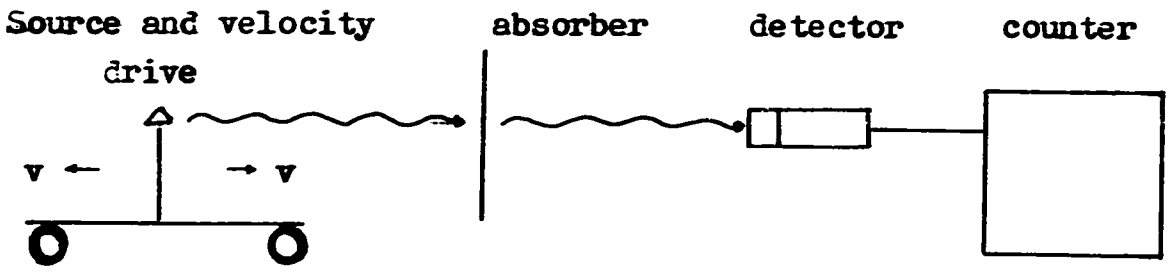


Fig. I-2 A basic setup in a Mössbauer Experiment.

B. Theory of Mössbauer Effect

It is interesting to find the reason why the gamma absorption increased when the temperature was lowered in the Mössbauer experiment. One important fact that emerges is that there is no longer a unique relation between the momentum of the gamma quantum and the recoil energy as it exists for free atoms, if an emitter or absorber atom forms part of a crystal lattice. Since the recoil energy is not sufficient to break the chemical bond in the lattice, it is given to the lattice as a whole and can only be radiated in the form of collective excitation quanta called "phonon". It may also be possible that no phonons are excited and then the recoil momentum is taken by the whole lattice mass instead of the mass of a single atom. Hence the actual magnitude of the recoil energy is much less than the natural line width $\Gamma$ . This small recoil energy ceases to interfere with the observation of resonance width D at half maximum given by the relation

$$D = \frac{1}{c}\sqrt{\frac{2kT}{m}}\ E_R$$

which disappears due to the large mass of the crystal lattice. Thus the Doppler broadening of resonance line drops out at the same time as the recoil energy and an undisplaced resonance line occurs with its natural width. Therefore, the probability of observing recoilless gamma resonance depends on the normal vibration spectrum of the lattice and on the probability of exciting different levels of the vibrations.

The lattice vibration spectrum is described by Debye's theory, in which the lattice has a continuum of oscillator states with different characteristic frequencies $\omega$ up to some maximum frequency $\omega_{max}$, which is determined by the number of oscillators N in the lattice volume V and characterized by the Debye temperature $\Theta$,

$$\hbar\omega_{max} = k\Theta \qquad \text{(I-1)}$$

k is Boltaman constant. In the case of an isotropic cubic crystal, $\omega$ and $\Theta$ are given approximately by equation

$$\hbar\omega_{max} = k\Theta \simeq \frac{2\pi u}{2d}\hbar \qquad \text{(I-2)}$$

where d is the lattice constant and u is the mean velocity of sound in the solid in question.

At extremly low temperatures ($T \approx 0$), there can be no transitions of oscillators from higher vibration levels to lower, since all the oscillators are in the lower levels and upper levels are empty. Accordingly, no energy can be

transferred from the crystal lattice to a gamma quantum incident on it. But even at zero temperature there is a possibility of oscillators jumping to higher levels using a part of the energy of the incident gamma quantum.

The probability of recoilless gamma resonance will drop with increase in temperature. Since phonons obey Bose-Einstein statistics, the greater the number of phonons already excited, the higher will be the probability of exciting new phonons from the recoil energy in emission and absorption of a gamma quantum. The probability f of a transition in which an individual nucleus receives the recoil energy without phonon excitation can be calculated in the Debye approximation

$$f = \exp\left\{-2\omega(T)\right\} \qquad \text{(I-3)}$$

f is called Debye-Waller temperature factor.

In low temperature range ($T \ll \Theta$), $\omega = (3/4)(E_R/k\Theta)$. For $E_R \leq 2k\Theta$, f reaches values that are nearly unity. At higher temperatures ($T \gg \Theta$), $\omega = (3/4)(E_R/k\Theta)(4T/\Theta)$ or $\omega \gg 1$ and the factor f is very small.

The classical theory of Mössbauer Effect developed by F. L. Shapiro (ref. 5) leads to a very simple interpretation of the Debye-Waller factor, namely,

$$f = \exp\left\{-\frac{\overline{x^2}}{\lambda\!\!\!^{-2}}\right\} = \exp\left\{-k^2 \langle x^2 \rangle\right\} \qquad \text{(I-4)}$$

where $2\pi\lambda\!\!\!^{-}$ is the wave length of the resonance gamma quanta

and $\overline{x^2}$ is the mean square deviation of a vibration of a vibrating atom in the lattice from its equilibrium position. Thus the Mössbauer line is well defined if the amplitude of the vibration of the atoms on the lattice is small in comparison with the wave length of the gamma radiation. This occurs principally at low temperatures.

A simple form of the equation for the recoil-free fraction may be derived for Einstein solid by expanding the exponential for case where $k^2 \langle x^2 \rangle \leq 1$. Using the properties of a harmonic oscillator, one can obtain

$$f = 1 - \frac{E_R}{\hbar \omega} \left( 1 + 2 n \right) \qquad \text{(I-5)}$$

Eq. I-5 indicates that the recoil free fraction will decrease with increasing temperature, since the total energy and n will increase according to

$$E_{total} = 3/2 \; kT = (n + \tfrac{1}{2}) \hbar \omega \qquad \text{(I-6)}$$

C. Description of experimental apparatus used to study Mössbauer Effect

A block diagram of the system used for the Mössbauer Effect experiment is given in Fig. I-3. Fig. I-4 gives the actual photographs of the system used for the experiment.

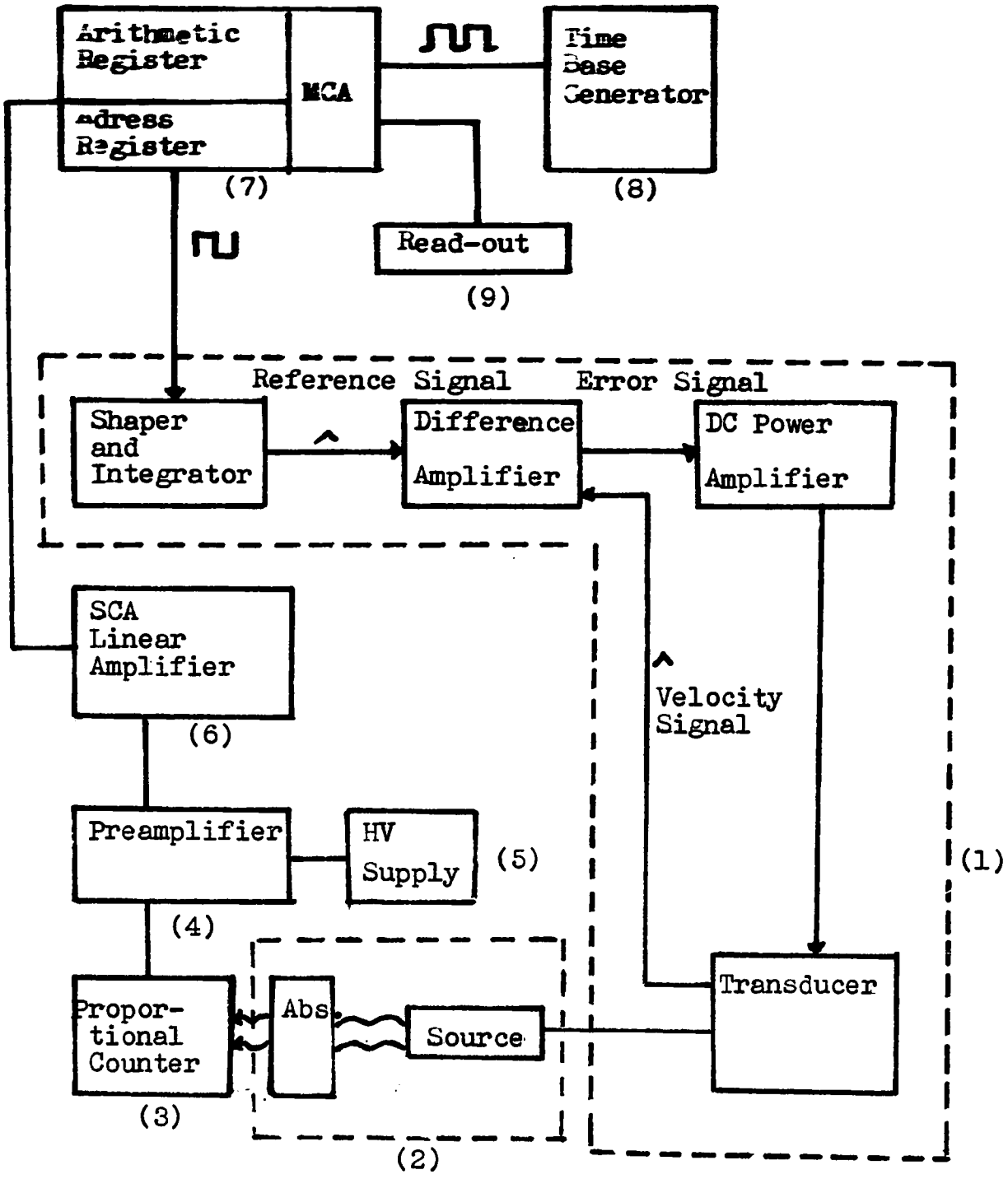


Fig. I-3 Block diagram of the system used for Mössbauer experiment. Numbers are used to label different components of the system.

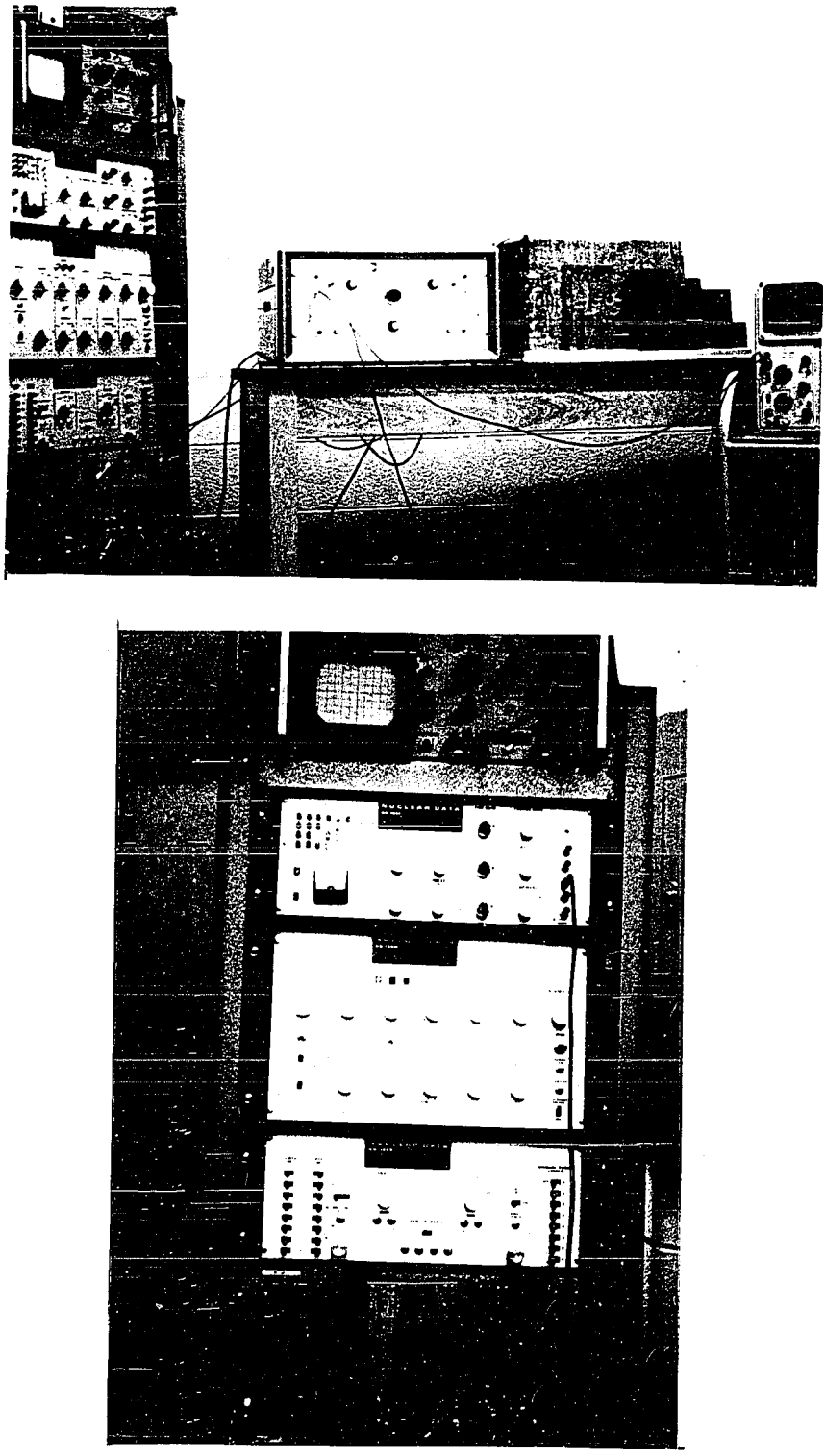

Fig. I-4 The photographs of the system used for the study of Mössbauer Effect.

A brief description of various components of the system shown in Fig. I-3 and Fig. I-4 is given below;

1. Mössbauer analyzer (NSEC Model AM-1)

This system consists of three units: (a) base plate, (b) transducer and (c) control unit.

(a) The base plate is a solid steel plate which provides a very rigid structure on which all of the mechanical parts, the transducer, absorber holder and a detector holder are mounted.

(b) The transducer is an electromechanical unit which provides the relative motion between the source and absorber required to produce Mössbauer Effect spectra. The transducer moves the source and at the same time produces a signal proportional to the velocity.

(c) The control unit is a solid state electronic unit which accepts a square wave signal from the address register of a multichannel analyzer. It contains shaper and integrator, difference amplifier and dc power amplifier required to drive the transducer. The velocity control unit is used to produce a velocity ($dx/dt$) varying linearly with time in a parabolic motion with constant acceleration ($d^2x/dt^2$). The displacement ($x$), as a function of time consists of segment of parabolas of positive and negative acceleration. The displacement, velocity and acceleration

of the parabolic mption as a function of time are illustrated in Fig. I-5.

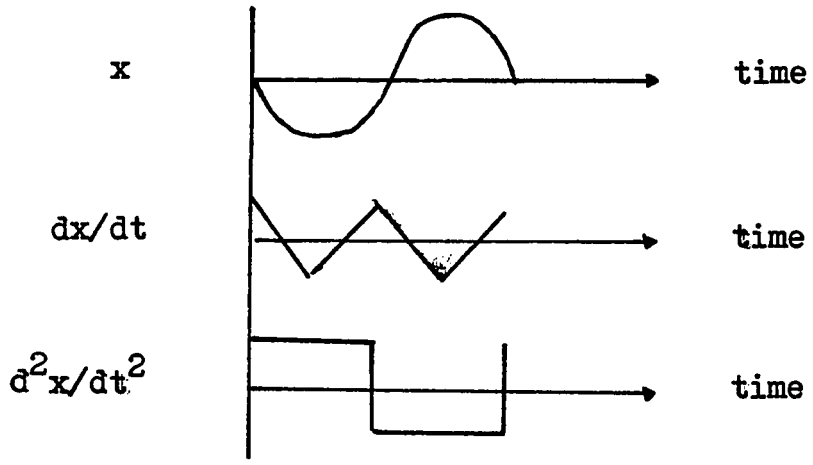


Fig. I-5 The displacement, velocity and acceleration as a function of time.

2. Source and absorber

The source foil of $Co^{57}$ in copper is mounted on the sample holder of the transducer. The absorber of iron compounds are mounted on the holder between the source and the detector (proportional counter).

3. Proportional counter (NSEC type 743)

The proportional counter is filled with a mixture of Xe-$CH_4$ gases. In the counter, part of the gamma-ray is transformed into an electric pulse proportional in height to the energy of the gamma-ray absorbed in the detector. These electrical pulses are fed into the preamplifier.

4. Preamplifier (Ortec Model 109)

The function of preamplifier is to reduce the impe-

dence of the system.

5. High voltage supply (PD Model 2k10)

This unit supplies a high voltage of the order of 2000 volts required for the proportional counter.

6. Single channel analyzer (HEWPACH Model 5528A)

The linear amplifier is used to amplify the analog pulses from the proportional counter. The single channel analyzer selects part of the pulse spectrum and produces pulses of standard size.

7. Multichannel analyzer (MCA)operable in the time mode (ND Model 180M)

The multichannel analyzer has 512 channels in the address register. It is used as a time analyzer to convert the velocity into channel numbers. The velocity signal is used to modulate linearly the amplitude of standardised pulses from a single channel analyzer set on the photopeak of interest. The modulated pulses whose amplitudes are proportional to velocity are sorted and stored in a multichannel analyzer by assigning an increment of velocity to each channel, and by having that channel accumulate counts only when the spectrometer is moving at the appropriate velocity. This velocity can be determined by using a signal generated by multichannel analyzer to drive the mechanical transducer.

The coincidence selector control in this unit is used to select a desirable energy from a total emitted gamma ray energy. When the specified gating signal is applied at the

"COINC" receptacle, it permits an input signal to be accepted for analysis.

8. Time base generator (ASA TU100A)

The synchronism between the mechanical motion and the analyzer is maintained by using the Mössbauer spectrometer analyzer with a multichannel analyzer driven in the time mode by a pulse generator. A square wave signal derived from the multichannel address register is used to produce a triangular reference signal by integration with additional operational amplifier. The signal produced in this manner provides the input for a velocity proportional to the reference signal.

9. Read-out device (ND 180 F)

The read-out device stores the measurement results within the system "memory" in digital form which can be observed in analog on a cathod-ray oscilloscope, and display an absorption spectrum, either during or after data accumulation. Stored data can also be read out in digital or analog for permanent record.

Synchronism between the channel and velocity as well as the square wave signal and the absorption spectrum are shown in Fig. I-6. Since the channel numbers are converted from the instantaneous velocity, the channel numbers shown in the figure are ladder shaped.

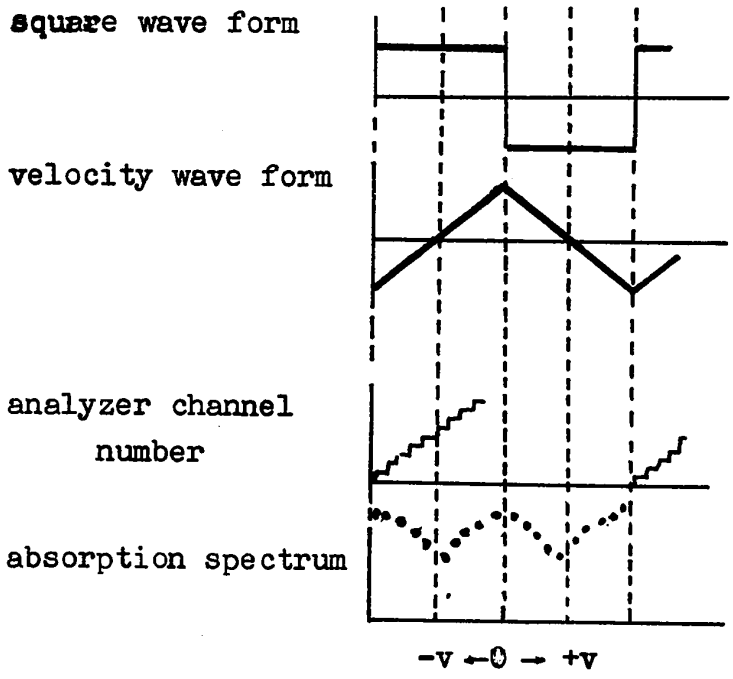


Fig. I-6 Synchronism between the square wave form, velocity wave form, analyzer channel number and absorption spectrum.

# Chapter II

## Hyperfine Interaction between the Nucleus and Its Surroundings

The Mössbauer spectrometer enables us to attain line widths which are small compared to the characteristic energies of interaction of nuclei with its surrounding electrons. Nuclear isomer shift, quadrupole interaction and magnetic hyperfine interaction are the three types of interactions between excited nucleus and its crystalline host, which have been studied in Mössbauer spectroscopy. The theoretical expressions for such interactions in terms of experimentally measurable parameters and electromagnetic multipole moments are given in the following sections.

A. Isomer shift

Isomer shift is an effect according to which the nuclear energy levels shift due to a change in Coulomb interaction resulting from a change in s-electron density, which may arises from a change in valence. This effect is sometimes called isotopic or chemical shift. In Mössbauer spectra, it manifests itself as a displacement of the resonance peak from the zero position on the velocity scale (Fig. II-1).

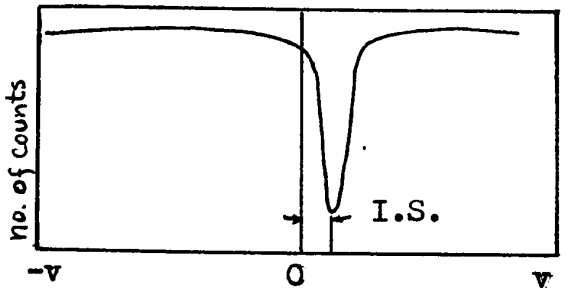


Fig. II-1 Isomer shift in the resonance absorption spectrum.

A theoretical expression for isomer shift can be written as

$$\text{I.S.} = \frac{4\pi}{5} Ze^2 \left\{ \psi_a^2(0) - \psi_s^2(0) \right\} R^2 \frac{\delta R}{R} \qquad \text{(II-1)}$$

where Z is the atomic number of the absorber, $e\psi_a^2(0)$ and $e\psi_s^2(0)$ are the electronic charge densities at the nucleus of the absorber and the source respectively, R is the nucleus radius and $\delta R$ is the difference between the nuclear radii of the excited state and ground state (See Appendix I for derivation of Eq.II-1).

The above expression for isomer shift consists of two factors. The first factor contains only a nuclear parameter $\delta R/R$; the second factor contains the electronic charge density at nucleus which is essentially a chemical parameter, since it is affected by the valence state of the atom.

It is obvious from Eq. II-1 that the experimental measurement of isomer shift will only give us the product of the above two atomic and nuclear parameters. Therefore, it is necessary to calculate one of the parameters from theoretical consideration in order to find the other parameter from the above expression.

B. Quadrupole splitting

Quadrupole splitting arises from the interaction between the nuclear quadrupole moment Q and the electric field gradient due to other charge in the crystal. Unlike isomer shift, this interaction does not shift the nuclear levels, but splits them. It lifts all or part of (2I + 1) fold degeneracy,

I being the nuclear spin quantum number. In the observed spectrum, quadrupole splitting manifests itself as seperation between the resonance maxima as shown in Fig. II-2.

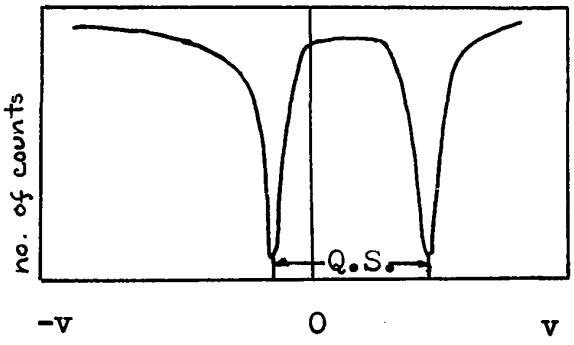


Fig. II-2 Quadrupole splitting in a Mössbauer Effect Spectrum.

For a nucleus with spin I = 3/2, the difference in the two eigenvalues of the quadrupole interaction corresponding to levels $m_I = 3/2$ and $m_I = 1/2$ is (Appendix I)

$$E_Q = \tfrac{1}{2} e^2 q Q (1 + \eta^2/3)^{\frac{1}{2}} \qquad \text{(II-2)}$$

$m_I$ being the magnetic quantum number; q and $q\eta$ being the electric field gradients; $\eta$ being the symmetric parameter; and Q being the excited state quadrupole moment. For positive q and eq $>0$, the state $|\pm 3/2\rangle$ lies above the state $|\pm 1/2\rangle$. For eq $< 0$, the reverse is true. Fig. II-3 explains the quadrupole splitting in $Fe^{57}$.

It should be noted that the measurement of quadrupole splitting only gives the product of the nuclear moment and the electric field gradient at the nucleus. To obtain the value for the quadrupole moment, an independent evaluation

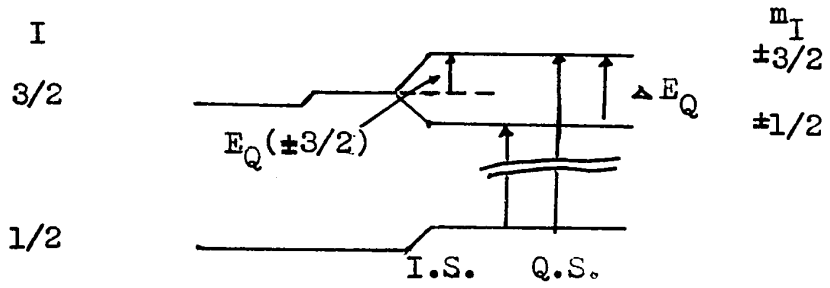


Fig. II-3 Quadrupolw splitting in $Fe^{57}$.

of the electric field gradient tensor is required.

C. Magnetic hyperfine interaction

This part of hyperfine structure is magnetic in character, which arises from the interaction of nuclear magnetic dipole moment $\mu$ with the magnetic field $\vec{B}$ due to the atom's own electrons. Magnetic hyperfine structure will be absent for nuclear levels with zero spin, since for such levles, the magnetic moment is zero. The magnetic hyperfine interaction can be written as (Appendix I)

$$E(m) = - g_I B \mu_N m \qquad \text{(II-3)}$$

with m = I, I-1, ....., -I.

Here I is the total spin; $\mu_N$ is the Bohr magneton, and $g_I$ is Linde's g factor of nuclear state I. Fig. II-4 explains the magnetic splitting in $Fe^{57}$.

For a single electron outside a nucleus, $\vec{B}$ can be expressed as

$$\vec{B} = g\beta\left\{\frac{\vec{l}}{r^3} + \frac{3\vec{r}(\vec{s}\cdot\vec{r})}{r^5} - \frac{\vec{s}}{r^3} + \frac{8\pi}{3}\vec{s}\delta(\vec{r})\right\} \qquad \text{(II-4)}$$

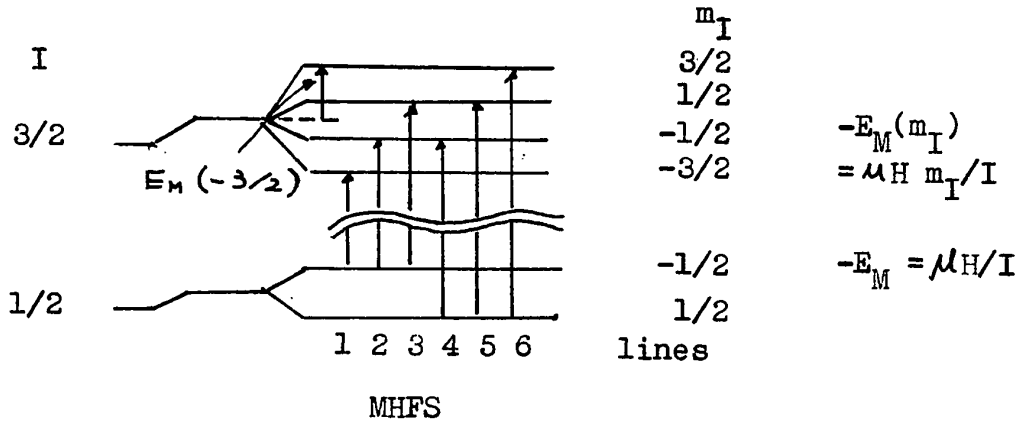


Fig. II-4 Magnetic hyperfine splitting in $Fe^{57}$.

when $\vec{B}$ in Eq. II-4 is substituted into Eq. II-3, the first term in E(m) gives the interaction of the nuclear magnetic moment with the current produced by the orbital electron; the second and third terms give the dipolar interaction between the nuclear and electronic spin; the fourth term is the Fermi contact term, which comes from the spin density at the nucleus, and is finite only for s-electron.

It is obvious that the magnetic hyperfine interaction in Eq. II-3 contains a nuclear parameter $\mu$ and an atomic parameter $\beta$ which can not be seperated experimentally. The same type of problem arises in isomer shift and quadrupole splitting. However, the situation is more favorable in this case because one can apply an external magnetic field and measure the resultant splitting.

# Chapter III

## Application of Mössbauer Effect Spectroscopy to the Study of Hyperfine Structure of $Fe^{57}$

A. Electronic configuration of $Fe^{57}$

The electronic configuration of a Mössbauer atom is directly related to its oxidation state and covalency, which are connected to isomer shift. Since the electric field gradient is mainly caused by the unsymmetric distribution of d electrons, it is also controlled by electric configuration.

A neutral iron atom has 26 electrons, which have the configuration,

$$1s^2\ 2s^2\ 2p^6\ 3s^2\ 3p^6\ 3d^6\ 4s^2$$

In a trivalent iron compound, the orbital configuration outside the argon core (18 electrons) is $3d^5$, while in the divalent is $3d^6$. The first 18 electron atom form a closed shell core and thus are spherically symmetric. The 3d shell consists of five orbitals which can accomodate a maximum of 10 electrons.

B. Isomer shift studies

The expression for isomer shift in Eq. II-1 mainly consists of two factors, one is a nuclear parameter $\delta R/R$, and the other is the electronic charge density of the atomic electrons at the nucleus. Thus by measuring isomer shift, one can easily find the value of either of the above two parameters, once the value of the other parameters is obtained by some other consideration.

The measurement of isomer shift provides us with the following information;

1. Oxidation state determination

A series of Mössbauer experiments done using some different iron salts as absorbers showed a systematic behavior with respect to isomer shift. The isomer shifts were measured for ionic salts of both divalent, $1s^2\ 2s^2\ 2p^6\ 3s^2\ 3p^6\ 3d^6$ and trivalent, $1s^2\ 2s^2\ 2p^6\ 3s^2\ 3p^6\ 3d^5$ irons. The divalent and the trivalent iron salts show a different isomer shift. This effect arises indirectly due to the 3s-electrons spending a fraction of their time further from the nucleus than the 3d-electrons. Thus the addition of 3d-electron increases the screening effect of the d-electron on 3s-electron and therefore reduces the charge density at the nucleus. From the above explanation, it is clear that the isomer shift of $Fe^{3+}$ compounds should be larger than that of $Fe^{2+}$ compounds.

2. Isomer shift in high-spin and partial covalent compound

As explained in the previous section (Chapter III, Section B.L.), the screening effect of 3d-electrons can affect the s-electron charge density at the nucleus. In the light of this screening effect, the isomer shift can be interpreted in terms of the effective charge ($\sigma$) of 3d-electrons. Assuming that the electronic configuration of iron compounds have the general form $3d^{8-\sigma-x}4s^x$, calibration graph between $\psi_s^2(0)$ and 4s-electron contribution can be drawn. Such a graph was first prepared by WWJ (ref. 6). A WWJ plot adapted from Spijkerman, Ruegg and May (ref. 7, 8) is shown in Fig. II-1. This graph is usally used to find the percentage of 4s-electron contribution of iron compounds of known isomer shift.

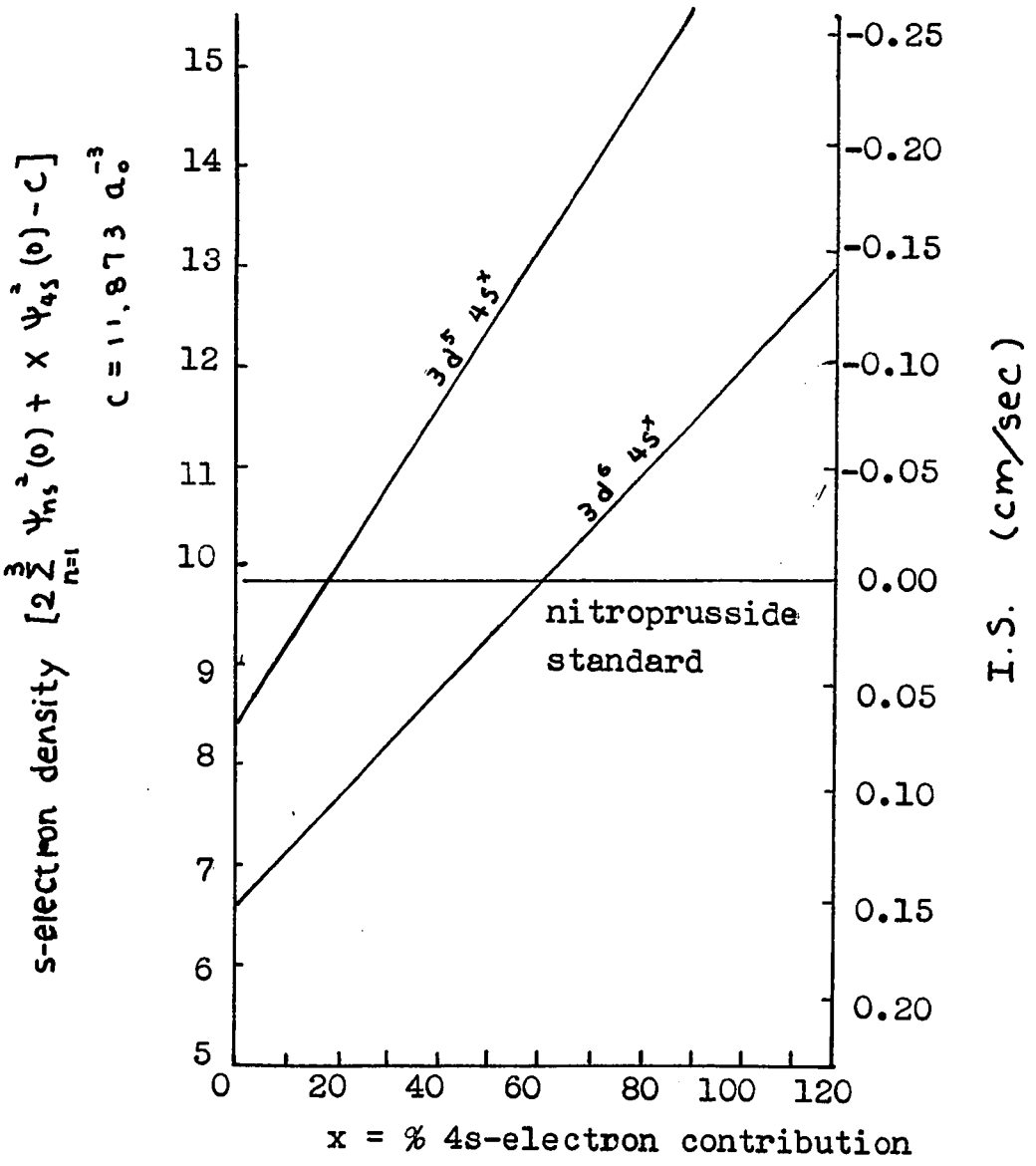


Fig. III-1 The calibration graph between s-electron density at nucleus and 4s-electron contribution

3. Calculation for $\delta_{R/R}$

As seen in previous chapter (Chapter II), the isomer shift and the s-electron density are related by

$$I.S. = \frac{4\pi}{5} Ze^2 \left\{ \psi_a^2(0) - \psi_s^2(0) \right\} R^2 \delta_{R/R}$$

The s-electron density at the nucleus of source and absorber can be determined from Hartree-Fock calculation for different configuration of multipole-ionized free ions. Substituting this density in the above equation, the value of $\delta R/R$ can be obtained. For iron it was found to be $-1.8 \times 10^{-3}$ (ref. 9).

4. Bonding relationship, especially with respect to bonding in covalent coordination compounds.

A ligand is a group attached to metal ion in complex. In the crystal field theory formulation of a metal complex, the ligands are considered as point charges or point dipoles. These constitute an electrostatic field, which has the symmetry of the complex. Here we are interested in the effect of the electrostatic field on the energies of the iron d-orbitals. In the bonding orbitals, some electronic charge from the ligands is transferred to the metal. This process is called ligand-to-metal $\pi$-bonding. The type of bonding which removes electronic density from the metal is called metal-to-ligand $\pi$-bonding, or back donation.

For high-spin iron complex with $\pi$-bonding ligands, the isomer shift varies with the increase of 4s-electron density when the ligands incline to give the electron to the Fe ion. For low-spin iron complex, there is a back donation of 3s-electron to $\pi^*$ anti-bonding orbitals of the ligands, and therefore the increase in s-electron density results in the reverse effect of ligands to that of high-spin complex.

C. Quadrupole splitting stu..es

1. The calculation of electric field gradient

In order to calculate electric field gradient $q$ and $q\eta$ in Eq. II-2, it is necessary to consider $q_v$ and $(q\eta)_v$ which are the contributions from the valence electrons, $q_l$ and $(q\eta)_l$ are the contributions from the lattice charges. According to Ingalls (ref. 10),

$$V_{zz}/e = q = (1-K)\, q_v + (1-\gamma_\infty)\, q_l$$
$$(V_{xx}-V_{yy})/e = q\eta = (1-K)\,(q\eta)_v + (1-\gamma_\infty)\,(q\eta)_v \qquad \text{(III-1)}$$

$(1-K)$ and $(1-\gamma_\infty)$ are the Sternheimer (ref. 11, 12, 13) shielding factors due to the polarization of the inner core electron by the valence and lattice charges.

The calculation of electric field gradient due to valence and lattice charges is given in Appendix II.

2. The quadrupole splitting in iron compounds

The outer electron configuration of free $Fe^{2+}$ ion is $3d^6$, which has a ground state of $^5D_4$. Five of the d-electrons form a spherical symmetry, and do not contribute to electric field gradient. The entire electric field gradient arises from the 6th electron. The ground state of $Fe^{3+}$ is $^6S_{5/2}$, which has the electron configuration of $3d^5$. Because of the spherical symmetry of the half-filled shell, the electrons do not produce field gradient. The observed small values of quadrupole splitting comes from the ionic charge of the lattice.

For covalent compounds with a coordination number 6, reverse situation is found. The typical quadrupole splitting of Fe(III) compounds are larger than those of Fe(II) compounds. The reason is that the effective atomic number of the iron atom in covalent ferrous compounds is 36. Two 3d electrons are used in forming six hybrid $d^2sp^3$ bonds, leaving three d-orbitals to be filled by ligand electrons. In octahedral ferri-complex compounds, the effective atomic number of iron is 35, the d-orbital vacancy provides a large value of electric field gradient at nucleus.

From above, we can see that quadrupole splitting provides the information on valence state and nature of chemical bond.

D. Magnetic hyperfine structure studies

1. The intensities of the lines

The transition between the excited state $I_e = 3/2$, and the ground state $I_g = 1/2$ of a magnetic dipole of angular momentum $L = 1$, is governed by the selection rules

$$\Delta m = 0, \pm 1$$

If $m_e$, M and $m_g$ are projection quantum numbers for $I_e$, L and $I_g$, respectively, the coupling of the angular momenta $I_e = 3/2$ and $I_g = 1/2$ through the magnetic dipole radiation field for $L = 1$ is given by a 3j-symbol

$$\begin{pmatrix} 3/2 & 1 & 1/2 \\ m_e & M & m_g \end{pmatrix}$$

In the presence of an internal magnetic field, six lines between two levels can be observed. The angular factor $F_L^M(\theta)$ is known as

$$F_1^0(\theta) = 3/2 \sin^2 \theta$$
$$F_1^{\pm 1}(\theta) = 3/4 (1 + \cos^2 \theta) \qquad \text{(III-2)}$$

$\theta$ being the angle between the axis of quantization and the direction of observation. Evaluating the 3j-symbol, the relative intensities of the various lines may be listed as in Tab. III-1.

| Lines | Relative intensities |
|---|---|
| 1, 6 | $(3/4) (1 + \cos^2 \theta)$ |
| 2, 5 | $\sin^2 \theta$ |
| 3, 4 | $(1/4) (1 + \cos^2 \theta)$ |

Tab. III-1 Relative intensities of six lines of magnetic hyperfine splitting.

In the absence of an external magnetic field, the six transitions averaging over all directions have intensities in the ratio 3 : 2 : 1 : 1 : 2 : 3. If the sample is partially magnetized, the ratio is 3 : $\beta$ : 1 : 1 : $\beta$ : 3, where $\beta$ has the value between 2 and 4 depending on the degree of magnetization.

2. Application

The Mössbauer spectroscopy provides the possibility of detecting magnetic exchange interactions and of determining the magnitude and the sign of the hyperfine magnetic field at selected sites within crystal. Through the study of magnetic hyperfine structure, the Curie point can also be rapidly and precisely determined. Further complications are always introduced by the interaction with quadrupole moment.

# Chapter IV

# Experimental Part

A. Description of the experimental arrangement

The source ($Co^{57}$) is mounted on the sample holder of the transducer, and is driven by an electromechanical system to produce a velocity varying linearly with time, so that equal time is spent in each velocity interval in the region of interest. The transmitted gamma ray pulse which is proportional in height to the energy of the gamma ray is then amplified. Part of the pulse spectrum of interest (14.4 keV peak) is selected by a single channel analyzer which produces unit pulses. A multichannel analyzer when operated in the multiscaler mode, counts each pulse from the single channel analyzer into the channel which is open at that moment.

The time base generator opens one channel after the other with precisely constant time intervals repetitiously. Synchronously with the repetitious scanning through the channel address scaler, a binary flip-flop in the analyzer address system switches from one memory half to the other, thus producing a square-wave signal. Then the crude signal is shaped with an operational amplifier to obtain a very accurate square-wave form.

From the electromechanical system driving the transducer, a velocity signal of triangular wave form is produced. The velocity is used to linearly modulate the amplitudes of standardized pulses from the single-channel analyzer. The modulated pulses whose amplitudes are proportional to velocity, are then sorted in a multichannel analyzer. The pulses counted by the multichannel analyzer display the entire velo-

city spectrum. The spectrum can be observed with the oscilloscope. The number of counts can be printed out with the printer.

B. Correction applied to the observed Mössbauer Effect spectra

1. Second-order Doppler correction

It is possible to have a shift in the observed spectrum due to the second order Doppler effect, if the source and the absorber are at different temperatures (ref. 14).

The expression for the Doppler effect (ref. 15) is

$$\nu_{source} = \nu_{obs} (1-vr \cos\theta/c)(1+v^2/2c^2) \qquad \text{(IV-1)}$$

Here $\nu$ is the frequency of the gamma ray energy, $\theta$ is the angle between the motion of source and the direction of observation. v is the velocity of emitting nucleus moving about the equilibrium position. When the time period of vibration of the nucleus is much less than the life-time of the excited state of the nucleus, the linear term ($vr \cos\theta/c$) in Eq. IV-1 will average out. The quadratic tern $v^2/2c^2$ will remain and cause a second-order Doppler shift. Therefore, we have

$$\begin{aligned}\nu_{source} &= \nu_{obs} (1+v^2/2c^2) \\ &= (\nu_{source} - \nu_{obs})/\nu_{obs} (v^2/2c^2) \qquad \text{(IV-2)}\end{aligned}$$

Thus the shift of energy due to the second-order Doppler effect can be written as

$$\nu_{Dopp} = \tfrac{1}{2} \frac{v^2}{c^2} E_\gamma \qquad \text{(IV-3)}$$

where $E_\gamma$ is the gamma ray energy.

Since the source and the absorber in our experiment were at the same temperature, the second-order Doppler shift correction was unnecessary.

2. Solid angle correction

The correction is necessary due to a small change in counts of spectrum data caused by the change in solid angle subtended at the absorber during Doppler motion. To apply this correction to the spectrum data in the computer program, the following equation were used

(correct no. of counts of nth channel)

= (no. of counts of nth channel)

$$\times \left( 1 \pm \frac{\text{(no. of counts of 384th channel)}}{\text{(no. of counts of 128th channel)}} \times \frac{n}{128} \right)^2$$

positive for $0 < n \leq 128$, negative for $256 < n \leq 384$;

(correct no. of counts of nth channel)

= (no. of counts of nth channel)

$$\times \left( 1 \pm \frac{\text{(no. of counts of 384th channel)}}{\text{(no. of counts of 128th channel)}} \times \frac{128 - n}{n} \right)^2$$

positive for $128 < n \leq 256$, negative for $384 < n \leq 512$.

These equations are derived from the relation between the velocity of moving source and the number of counts of each channel of the spectrum data.

The geometric relation between the solid angle $\Omega$ of emission relative to the absorber and the relative position r between source and the absorber gives

$$(\Omega+\Delta\Omega)/\Omega = r^2/(r+\Delta r)^2$$

where $\Delta\Omega$ and $\Delta r$ are the changes in the solid angle and the source-absorber distance, and displacement of the source during Doppler motion, respectively. This is shown in Fig. IV-1.

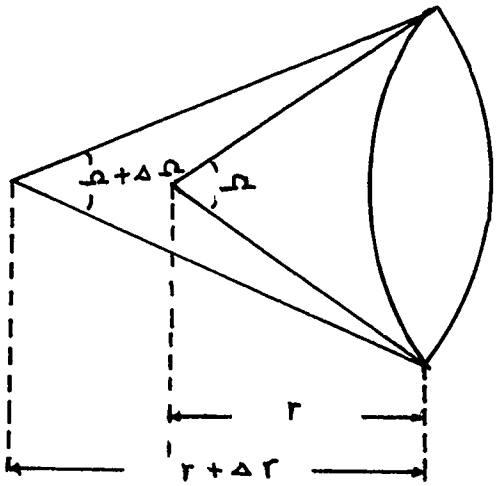


Fig. IV-1 Source-absorber distance and the solid angle of emission relative to the absorber.

The moving source has maximum velocity at equilibrium position and zero velocity at maximum displacement. Assuming that the intensity of transmitted gamma ray photon through the absorber is constant for the energy within the range of velocity scale of observation, as in Fig. IV-2, the square root of the number of counts in each channel increases linearly from A at velocity -v to maximum point B at zero velocity, then decreases to the point C at velocity +v, and changes symmetrically from velocity scale +v to -v through C,D and E.

We assume that c is the number of counts of one of the spectrum data, when the source is at equalibrium position, $\Delta$ c is the change in number of counts corresponding to displacement

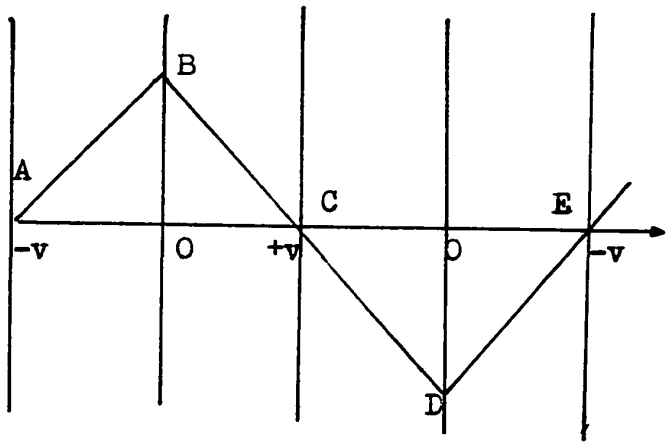


Fig. IV-2 The lineality of the relation between the square root of no. of counts and the velocity scale.

$\Delta r$ of the source. For a point between the position of maximum displacement in either direction and the equilibrium position of the source, we have

$$\Delta r = kv^2 \qquad \text{(IV-4)}$$

k being the proportionality constant. The probability of transmission is proportional to the square of the counts, and from Eq. IV-4 we can write

$$\frac{\Omega+\Delta\Omega}{\Omega} = \frac{r^2}{(r+\Delta r)^2} = \frac{r^2}{(r+kv^2)^2} = \frac{c^2}{(c+\Delta c)^2}$$

this gives

$$v^2 = \text{constant} \times \Delta c \qquad \text{(IV-5)}$$

This relation leads to the equation for the correction of spectrum data.

3. Curve fitting to Mössbauer Effect spectra

Due to some irregularity in the motion of the source and the random nature of decay process in the detector, the spectral data on the gamma ray resonant absorption are generally scattered, such that the outline of the specta are not smooth curves, For this correction, a Laurentian outline of resonant absorption is assumed, given by

$$L(n_x) = \frac{A\,\Gamma}{\Gamma^2 + (n_p - n_x)^2} \qquad \text{(IV-1)}$$

A being the amplitude, $n_x$ the channel number; $n_p$ the channel number of peak position, and $\Gamma$ being the half width of resonant absorption line.

A least square method was applied to minimize the uncertainty in the experimental data, and the best fit Laurentian curve was found with the help of CDC (3300) computer at Sir George Williams University.

C. Experimental results and discussion

1. Calibration of the velocity scale

To measure the magnitude of isomer shift and quadrupole splitting in the corrected spectrum, calibration of the velocity scale is necessary, since the velocity of the source set on the spectrometer may not be its real velocity. For the calibration of the velocity scale, generally an

absorber of known transitional energy is used as a standard. For instance, in the case of metallic iron, magnetic hyperfine splitting occurs at the velocities $g_0$ = 0.3924 cm/sec for the ground state, and $g_1$ = 0.2244 cm/sec for the excited state. These velocities can be determined by nuclear magnetic resonance study. Thus, when iron is used for calibration, one can easily determine the number of channels n existing between the third and fourth peaks in the spectrum, which in fact corresponds to the third and fourth transition lines shown in Fig. III-1 in Chapter III. The energy difference between these lines is $g_0 - g_1$ = 0.1680 cm/sec. Dividing this energy difference by the channel number n, one can establish the correspondence between velocity scale and the various channels.

2. Measurements of isomer shift and quadrupole splitting

Tab. IV-1 gives the observed values of isomer shift and quadrupole splitting in units of cm/sec. Column 1 in this table gives the chemical formulae of compounds used as absorbers; in column 2 are given the observed isomer shift with respect to sodium nitroprusside; and the observed quadrupole splitting in different compounds are given in column 4.

| Chemical formulae of the absorbers | I. S. with respect to $Co^{57}$ in Cu (cm/sec) | I. S. with respect to sodium nitroprusside (cm/sec) | Q. S. (cm/sec) |
|---|---|---|---|
| $FeSO_4 \cdot 7H_2O$ | 0.101 | 0.150 | 0.274 |
| $FeCl_2 \cdot 4H_2O$ | 0.098 | 0.147 | 0.286 |
| $Fe_2(SO_4)_3 \cdot 9H_2O$ | 0.021 | 0.070 | 0.050 |
| $FeCl_3 \cdot 6H_2O$ | 0.014 | 0.063 | 0.068 |
| $Fe(NO_3)_3 \cdot 9H_2O$ | 0.013 | 0.062 | 0.070 |
| $Fe_2O_3$ | 0.007 | 0.056 | 0.014 |
| $K_4Fe(CN)_6 \cdot 3H_2O$ | -0.027 | 0.022 | 0 |
| $Na_2Fe(CN)_5NO \cdot 2H_2O$ | -0.049 | 0 | 0.169 |

Tab. IV-1 observed values of isomer shift and quadrupole splitting of different iron compounds.

3. The calculation of electronic charge density at nucleus from observed isomer shift

The constant factor C in the equation

$$I.S. = C \times \frac{\delta R}{R} \times \left\{ \psi_a^2(0) - \psi_s^2(0) \right\} S(Z) \qquad (VI-2)$$

has been calculated by Shirley (ref. 16) and can be expressed as

$$C = \frac{4\pi Z e^2 R^2 c}{5 E_\gamma}$$

$$= 15.6 \times 10^{-26} \times Z A^{2/3} E_\gamma^{-1} \quad cm^4/sec \qquad (E_\gamma \text{ in keV})$$

For $Fe^{57}$, the atomic number is Z = 26, the mass number is A = 57, and $E_\gamma$ = 14.4 keV, this gives

$$C = 4.1787 \times 10^{-24} \text{ cm}^4/\text{sec}$$

S(Z) is the relativity correction factor and is equal to 1.32 for iron (ref. 17).

Using sodium nitroprusside as standard substance, and substituting in Eq. IV-2 the measured values of isomer shift in column 3 of Tab. IV-1, the constant C, S(Z) and $R/R = -1.8 \times 10^{-3}$ from the theory of shell model, the electronic charge densities at nucleus in various compounds relative to sodium nitroprusside were calculated. These values are given in column 3 of Tab. IV-2.

| Chemical formulae of the absorbers | $\psi_a^2(0) - \psi_{SNP}^2(0)$ $(a_o^{-3})$ | $\psi_a^2(0)$ $(a_o^{-3})$ |
|---|---|---|
| $FeSO_4 \cdot 7H_2O$ | -2.36 | 11880.54 |
| $FeCl_2 \cdot 4H_2O$ | -2.20 | 11880.78 |
| $Fe_2(SO_4)_3 \cdot 9H_2O$ | -1.06 | 11881.74 |
| $FeCl_3 \cdot 6H_2O$ | -0.95 | 11881.81 |
| $Fe(NO_3)_3 \cdot 9H_2O$ | -0.94 | 11881.84 |
| $Fe_2O_3$ | -0.84 | 11881.96 |
| $K_4Fe(CN)_6 \cdot 3H_2O$ | -0.33 | 11882.47 |
| $Na_2Fe(CN)_5NO \cdot 2H_2O$ | 0 | 11882.80 |

Tab. IV-2 Electronic charge densities at nucleus in different iron compounds. $a_o$ stands for the atomic unit and is equal to 0.5292 Å.

From the calibration curve of WWJ plot (ref. 8), the electronic charge density at nucleus in sodium nitroprusside is estimated to be 11882.80 $a_o^{-3}$, where $a_o$ is the atomic unit and is equal to 0.5292 Å. Adding this value to column 3 in Tab. IV-2, the electronic charge densities in different compounds were obtained and are given in column 4 of this table. A sample of the above calculation is given in Appendix III.

By using Roothaan-Hartree-Fock method (ref. 18, 19, 20, 21, 22, 23, 24), the electronic charge density at nucleus of s-electron can be calculated from the wave function,

$$\Psi_{i\lambda\alpha} = \sum_p C_{i\lambda p} \left[(2n_{\lambda p})!\right]^{-\frac{1}{2}} (2\zeta_{\lambda p})^{n_{\lambda p}+\frac{1}{2}} r^{n_{\lambda p}-1} e^{-\zeta_{\lambda p} r} \cdot Y_{\lambda\alpha}(\theta, \phi)$$

More detail about this wave function as well as the sample calculation of electronic charge density at nucleus is given in the Appendix IV.

Fig. IV-3 gives the calibration curves of 4s-electron percentage contribution for different iron compounds. These curves are obtained from the modification of WWJ (ref. 8) curve.

The values of 4s-electron percentage contribution for each compounds obtained from this graph is given in Tab. IV-3.

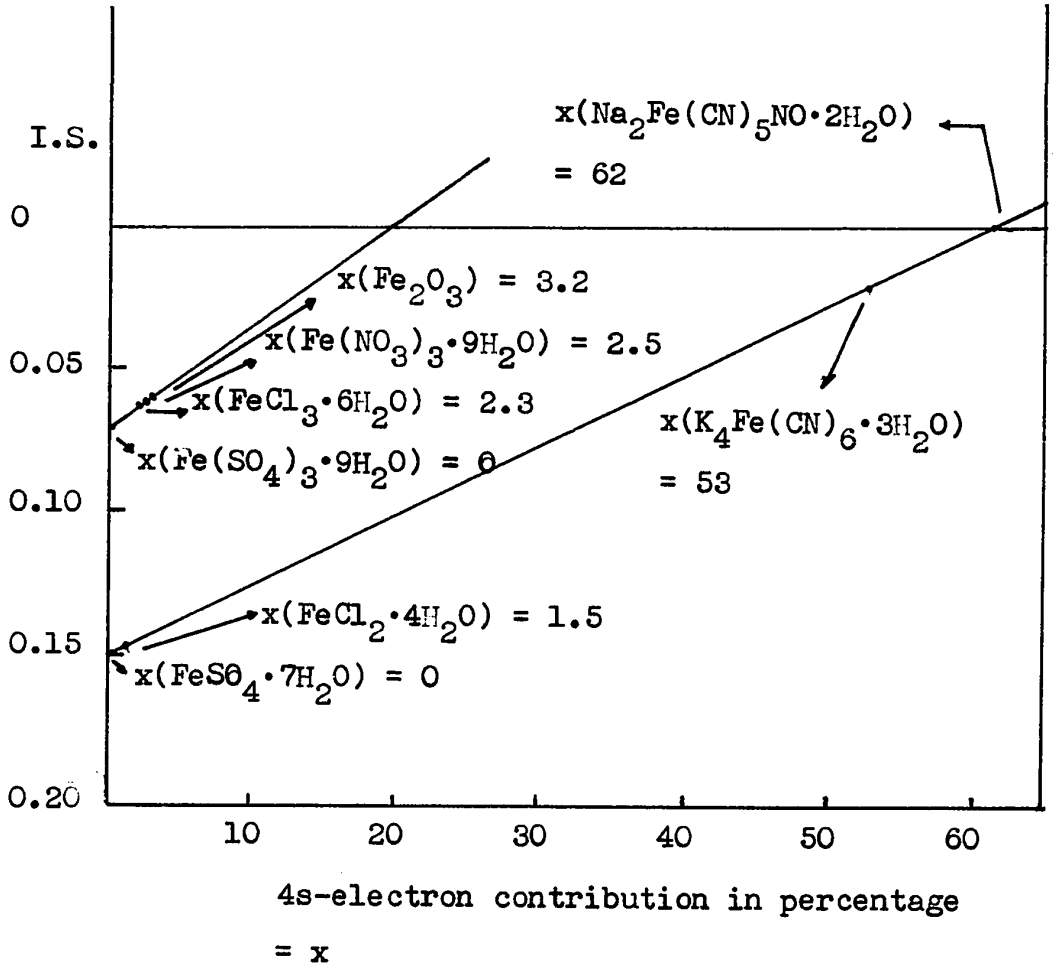


Fig. IV-3 Calibration curve of 4s-electron percentage contribution.

| Chemical formulae of the absorbers | 4s-electron percentage contribution |
|---|---|
| $FeSO_4 \cdot 7H_2O$ | 0 |
| $FeCl_2 \cdot 4H_2O$ | 1.5 |
| $Fe_2(SO_4)_3 \cdot 9H_2O$ | 0 |
| $FeCl_3 \cdot 6H_2O$ | 2.3 |
| $Fe(NO_3)_3 \cdot 9H_2O$ | 2.5 |
| $Fe_2O_3$ | 3.2 |
| $K_4Fe(CN)_6 \cdot 3H_2O$ | 53.0 |
| $Na_2Fe(CN)_5NO \cdot 2H_2O$ | 62.0 |

Tab. IV-3 4s-electron percentage contribution for different compounds.

The theoretical electronic charge densities at nucleus are given in column 2 of Tab. IV-4. The percentage difference between calculated electronic charge densities and empirical values found in this investigation are given in column 4. A sample calculation is given in Appendix IV.

3. Explanation of the discrepancy of the results

The theoretically calculated charge densities are slightly higher than the empirical values. The discrepancy may be due to partial neglect or too low estimation of the effect of d- and p-orbitals to the inner s-orbitals by Roothaan-Hartree-Fock method. The charge density is of the order of the square of the magnitude of wave function.

| Chemical formulae | Calculated electronic charge densities at nucleus ($a_o^{-3}$) | Empirical values of electronic charge densities at nucleus ($a_o^{-3}$) | Percentage difference between the values in column 2 and 3 |
|---|---|---|---|
| $FeSO_4 \cdot 7H_2O$ | 11898.65 | 11880.54 | 0.160 |
| $FeCl_2 \cdot 4H_2O$ | 11898.69 | 11880.78 | 0.159 |
| $Fe_2(SO_4)_3 \cdot 9H_2O$ | 11900.11 | 11881.74 | 0.163 |
| $FeCl_3 \cdot 6H_2O$ | 11900.22 | 11881.81 | 0.163 |
| $Fe(NO_3)_3 \cdot 9H_2O$ | 11900.23 | 11881.84 | 0.163 |
| $Fe_2O_3$ | 11900.27 | 11881.96 | 0.164 |

Tab. IV-4 The theoretical values of electronic charge densities at the nucleus in different compounds.

Therefore, a small change in wave function will likely introduce an appreciable change in electronic charge density.

4. Quadrupole splitting in Fe compounds and the electric field gradient

Comparing the quadrupole splitting of different absorbers, one can see that the splitting for trivalent compounds is much smaller than that for divalent compounds. This can be explained by the fact that the high spin compounds of half-filled d-orbitals in trivalent iron compounds have zero contribution from d-orbitals, and therefore, the quadrupole splitting for such compounds must come from the lattice charge.

The observed zero quadrupole splitting for $K_4Fe(CN)_6 \cdot 3H_2O$ indicates that the iron atom is surrounded by six equivalent bonds, resulting in a spherically symmetric charge distribution which causes the absence of quadrupole splitting. The weak splitting in the case of $Na_2Fe(CN)_5NO \cdot 2H_2O$ is due to the presence of $NO^+$ ion and the disturbance of spherically symmetric charge distribution by $NO^+$.

Putting the values of excited state quadrupole moment

$Q = 0.29 \times 10^{-24}$ cm$^2$ in the equation

$$Q.S. = \frac{e^2 q Q}{2} (1 + \eta^2/3)^{\frac{1}{2}},$$

values of $q (1 + \eta^2/3)^{\frac{1}{2}}$ for each iron compound calculated are given in column 3 of Tab. IV-5.

| Chemical formulae of the absorbers | Q.S. in eV x $10^{-8}$ | eq $(1 + \eta^2/3)^{\frac{1}{2}}$ in V/cm$^2$ x $10^{17}$ |
|---|---|---|
| $FeSO_4 \cdot 7H_2O$ | 11.86 | 8.176 |
| $FeCl_2 \cdot 4H_2O$ | 12.76 | 8.804 |
| $Fe_2(SO_4)_3 \cdot 9H_2O$ | 2.26 | 1.559 |
| $FeCl_3 \cdot 6H_2O$ | 2.97 | 2.049 |
| $Fe(NO_3)_3 \cdot 9H_2O$ | 3.07 | 2.118 |
| $Fe_2O_3$ | 0.61 | 0.420 |
| $K_4Fe(CN)_6 \cdot 3H_2O$ | 0 | 0 |
| $Na_2Fe(CN)_5NO \cdot 2H_2O$ | 7.39 | 5.099 |

Tab. IV-5 The Q. S. and the values of $q (1 + \eta^2/3)^{\frac{1}{2}}$

5. The calculation of quadrupole splitting for divalent iron compounds.

In the ionic divalent iron compounds, it is assumed that the electric field gradient $q_l$ due to the lattice charge gives a minor contribution, and therefore can be neglected. The quadrupole splitting in ferrous compounds can be expressed as (see Appendix II),

$$Q.S. = \frac{e^2 q Q}{2} (1-K) \langle r^{-3} \rangle_{3d} \alpha^2 F(\Delta_1, \Delta_2, T)$$

Using $Q = 0.29 \times 10^{-24}$ cm$^2$, $K = 0.32$ (ref. 10), $\langle r^{-3} \rangle_{3d} = 4.8\ a_o^{-3}$, the ground state orbitals, covalency parameters (ref. 9), and splitting parameters (ref. 10) the quadrupole splitting are calculated and given in Tab. IV-5.

| Chemical formulae of the compounds | Ground state d-orbitals | $\alpha$ | $\Delta_1$ | $\Delta_2$ | Calculated Q.S. (cm/sec) |
|---|---|---|---|---|---|
| $FeSO_4 \cdot 7H_2O$ | $d_{xy}$ | 0.08 | 480 | 1300 | 0.353 |
| $FeCl_2 \cdot 4H_2O$ | $d_{x^2-y^2} - 0.01 d_{z^2}$ | 0.08 | 750 | 2900 | 0.367 |

Tab. IV-5 Quadrupole splitting of divalent compounds

The difference of the calculated values and the observed values of quadrupole splitting may be due to the absence of contribution from electric field gradient due to the lattice charges. Comparing the quadrupole splitting of

the two compounds in Tab. IV-1 and Tab. IV-5, it is clear that the contribution of electric field gradient due to the lattice in these compounds are close to each other.

6. Calculation of internal magnetic field

For $Fe_2O_3$, the six spectrum lines are not uniformly distributed as for $Fe^{57}$. There is a perturbation due to quadrupole interaction. The energy levels due to the combined effect of magnetic hyperfine interaction, the quadrupole interaction and the isomer shift are shown in Fig. IV-4.

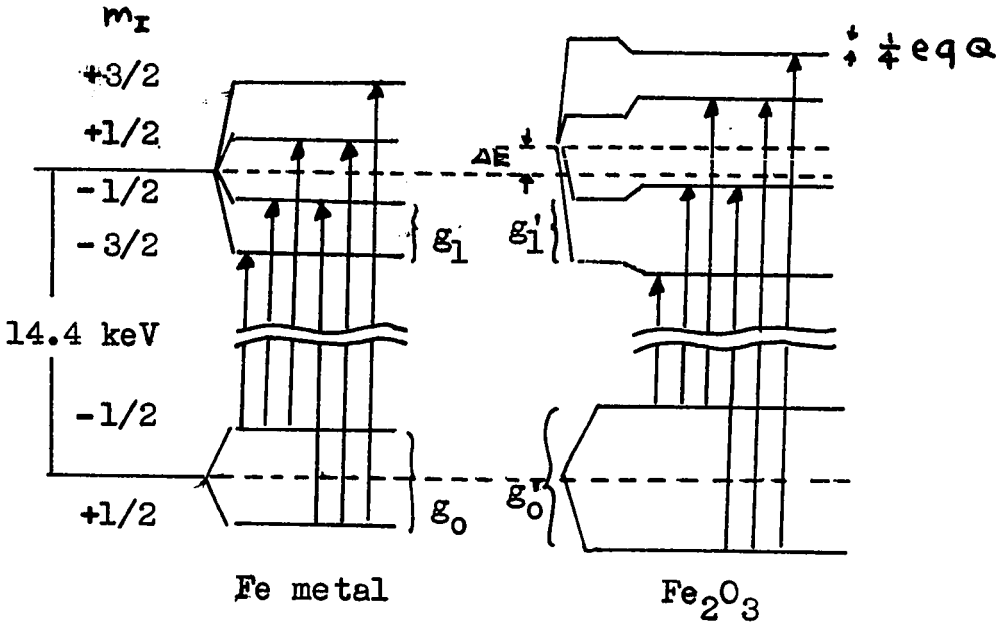


Fig. IV-4 Schematic energy levels of Fe and $Fe_2O_3$.

The values of $g_0'$ and $g_1'$ measured for $Fe_2O_3$ are

$g_0' = 0.345$ cm/sec

$g_1' = 0.615$ cm/sec

At room temperature the internal magnetic field in metallic

iron is 333 kOe (ref. 25). Therefore, using the relation

$$g_o'/g_o = H/333$$

$$g_1'/g_1 = H/333$$

with H in kOe, the internal magnetic field of $Fe_2O_3$ is found to be 515 kOe. This value is in good agreement with that obtained by Kistner and Sunyar (ref. 9).

# Appendices

# Appendix I

## Nuclear Hyperfine Interaction

The Coulomb interaction Hamiltonian between the nucleus and electron is given by

$$H(E) = \sum_{e,n} \frac{e_n e_e}{|\vec{r}_n - \vec{r}_e|} \qquad \text{(A1-1)}$$

where the subscript n and e refer to the nucleus and electrons, respectively. The multipole expansion of $\frac{1}{|\vec{r}_n - \vec{r}_e|}$ for $|r_e| > |r_n|$ gives

$$\frac{1}{|\vec{r}_n - \vec{r}_e|} = 4\pi \sum_{L=0}^{\infty} \sum_{M=-L}^{L} \frac{1}{2L+1} \frac{r_n^L}{r_e^{n+1}} Y_L^M(\theta_n, \phi_n)\, Y_L^M(\theta_e, \phi_e) \qquad \text{(A1-2)}$$

$Y_L^M(\theta, \phi)$ being the spherical harmonics.

According to the definition of the electric multipole moment,

$$M_\mu(EL) = \sum_k e_k |r_k|^2 Y_L^M(\theta_k, \phi_k) \qquad \text{(A1-3)}$$

The electrostatic interaction Hamiltonian is given by

$$H(E) = 4\pi \sum_{L=0}^{\infty} \frac{1}{2L+1} \sum_{M=-L}^{L} (-1)^L M_M(EL)\, V_{-M}(EL) \qquad \text{(A1-4)}$$

where the spherical field tensor $V_M(EL)$ is defined as

$$V_M(EL) = \sum_e \frac{e_e}{r_e^{L+1}} Y_L^M(\theta_e, \phi_e) \qquad \text{(A1-5)}$$

A. Monopole interaction

For monopole interaction L = 0, the Hamiltonian in Eq. A1-4 is given by,

$$H(E0) = Z\, e \sum_e \frac{e_e}{r_e} \qquad \text{(A1-6)}$$

This interaction causes a shift of all nuclear levels, which is not generally observed. The derivation of this interaction is based on the assumption $|r_e| < R$, R being the nuclear radius. As a matter of fact, the wave function of atomic electron does not vanish inside the nucleus. Therefore, we assume that the energy shift depending on the charge distribution inside the nucleus, is caused by the interaction between the electon charge density and the nuclear charge density inside the nucleus.

The electrostatic interaction energy between the electron charge density $e\rho_e(r_e)$ and the nuclear charge density $e\rho_n(r_n)$ inside the nucleus is,

$$E(0) = -e^2 \iint \frac{\rho_n(r_n)\, \rho_e(r_e)}{r_e} \, d\tau_e \, d\tau_n \qquad \text{(A1-7)}$$

If the density $\rho(r)$ is averaged over a sphere of radius r, such that

$$\rho'(0) = \frac{1}{4\pi} \iint \rho(r) \sin\theta \, d\theta \, d\phi \qquad \text{(A1-8)}$$

then E(0) becomes,

$$E(0) = -(4\pi e)^2 \iint \frac{\rho_n'(r_n)\, \rho_e'(r_e)}{r_e} \, r_e^2 \, dr_e \, r_n^2 \, dr_n$$

$$= -\left(4\pi e^2\right) \int_o^{\infty}\int_o^{r} \left(\frac{1}{r_n} - \frac{1}{r_e}\right) \rho_e'(r_e)\rho_n'(r_n)$$

$$r_e^2 \, dr_e \, r_n^2 \, dr_n + E_o \qquad \text{(A1-9)}$$

where $E_o$ is just the Coulomb energy for a point nucleus and can be written as

$$E_o = -Z e^2 \int \frac{\rho_e'(r_e)}{r_e} \, d\tau_e \qquad \text{(A1-10)}$$

Let us consider the density in the nuclear region only, $\rho_e'(r_e)$ then becomes

$$\rho_e'(0) = e\,\psi^2(0) \qquad \text{(A1-11)}$$

The difference between the interactions E(0) and $E_o$ is

$$\delta E = \frac{8\pi}{3} e^2 \psi^2(0) \int r_n^4 \rho_n'(r) \, dr_n$$

$$= \frac{2}{3}\pi e^2 Z \psi^2(0) \langle r_n^2 \rangle \qquad \text{(A1-12)}$$

If the nucleus with radius R is uniformly charged

$$\langle r_n^2 \rangle = \frac{3}{5} R^2$$

and Eq. A1-12 can be written as

$$\delta E = \frac{2}{5}\pi Z e^2 R^2 \psi^2(0) \qquad \text{(A1-13)}$$

For nuclear transition from level b to a, the change $\delta E$ is shown in Fig. A1-1.

The difference in quantity $\Delta(\delta E)$ between the source and the absorber gives rise to the isomer shift and the expression for it is;

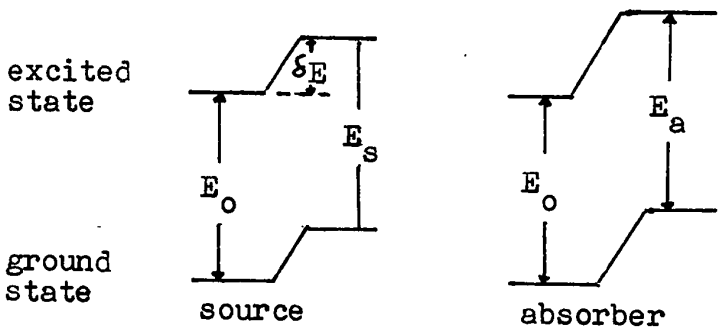


Fig. A1-1 The origin of isomer shift

$$\text{I.S.} = \frac{2}{5} Z e^2 \left\{ R_e^2 - R_g^2 \right\} \left\{ \psi_b^2(0) - \psi_a^2(0) \right\} \qquad \text{(A1-14)}$$

Subscripts e and g refer to an excited and a ground state of the nucleus, respectively. If $\delta R$ is the difference between $R_e$ and $R_g$

$$\text{I.S.} = \frac{4}{5} Z e^2 \left\{ \psi_a^2(0)_{\text{absorber}} - \psi_s^2(0)_{\text{source}} \right\} R^2 \frac{\delta R}{R} \qquad \text{(A1-15)}$$

B. Quadrupole interaction

Taking the higher order term (L = 2) for quadrupole moment in the electrostatic interaction Hamiltonian of Eq. A1-4, we have

$$H_Q(E2) = \frac{4\pi}{5} \sum_{M=-2}^{M=2} (-1)\, M_M(E2)\, V_{-M}(E2) \qquad \text{(A1-16)}$$

The matrix element of $H_Q$ is given by

$$\langle Im' \mid H(E2) \mid Im \rangle$$

$$= \frac{4\pi}{5} (-1)^{I-m'+M} \begin{pmatrix} I & 2 & I \\ -m' & M & m \end{pmatrix} \langle I \mid M(E2) \mid I \rangle$$

$$\times V_{-M}(E2)$$

m being the magnetic quantum number. If the electrostatic field is quantized with respect to z axis fixed in space, and $\phi$ is defined as the electrostatic potential at the nucleus, then in Eq. A1-5,

$$V_{\pm 1}(E2) = 0$$

$$V_{+2}(E2) + V_{-2}(E2) = \frac{1}{3}\sqrt{\frac{15}{8\pi}} \left(\frac{\partial^2\phi}{\partial x^2} - \frac{\partial^2\phi}{\partial y^2}\right)$$

$$V_0(E2) = \frac{1}{4}\sqrt{\frac{5}{\pi}} \frac{\partial^2\phi}{\partial z^2} \qquad \text{(A1-18)}$$

therefore,

$$\langle Im' \mid H(E2) \mid Im \rangle$$

$$= (-1)^{-1} \left\{ \sqrt{\frac{\pi}{5}} \begin{pmatrix} I & 2 & I \\ -m' & 0 & m \end{pmatrix} \times \langle I \mid M(E2) \mid I \rangle \frac{\partial^2\phi}{\partial z^2} \right.$$

$$+ \sqrt{\frac{15}{8\pi}} \begin{pmatrix} I & 2 & I \\ -m & 2 & m \end{pmatrix} \times \langle I \mid M(E2) \mid I \rangle$$

$$\left. \frac{1}{3} \left(\frac{\partial^2\phi}{\partial x^2} - \frac{\partial^2\phi}{\partial y^2}\right) \right\} \qquad \text{(A1-19)}$$

The definition of quadrupole moment gives

$$eQ = 4\sqrt{\frac{\pi}{5}} \langle II \mid M_0(E2) \mid II \rangle \qquad \text{(A1-20)}$$

$$= 4\sqrt{\frac{\pi}{5}} \frac{2I\,(2I-1)^{\frac{1}{2}}}{[(2I+3)(2I+2)(2I+1)2I]^{\frac{1}{2}}} \langle I \mid M(E2) \mid I \rangle$$

On evaluating the 3j-symbols and substituting, we obtain the

expression for quadrupole interaction

$$E(M_I) = \langle Im \mid H(E2) \mid Im \rangle$$

$$= \frac{eqQ}{4I\,(2I-1)} \left[ 3m_I^{\,2} - I\,(I+1) \right] \left(1 + \frac{\eta^2}{3}\right)^{\frac{1}{2}} \qquad \text{(A1-21)}$$

where $\eta$ is the symmetry parameter defined by

$$= \frac{\frac{\partial^2 \phi}{\partial x^2} - \frac{\partial^2 \phi}{\partial y^2}}{\frac{\partial^2 \phi}{\partial z^2}}$$

C. Magnetic interaction

The magnetic moment $\mu_1$ is expressed as

$$\mu_1 = \sqrt{\frac{4\pi}{3}} \langle II \mid M_o(M1) \mid II \rangle$$

$$= \sqrt{\frac{4\pi}{3}} \begin{pmatrix} I & 1 & I \\ -I & 0 & I \end{pmatrix} \langle I \mid M(M1) \mid I \rangle$$

$$= \sqrt{\frac{4\pi}{3}} \frac{I}{\left[(2I+1)(I+1)I\right]^{\frac{1}{2}}} \langle I \mid M(M1) \mid I \rangle \qquad \text{(A1-22)}$$

M(M1) is a vector operator of static dipole moment and can be written in the form

$$\vec{\mu}_J = g_I \mu_N I \qquad \text{(A1-23)}$$

The Hamiltonian of the interaction between a magnetic dipole moment $\mu$ and a magnetic field $\vec{B}$ is,

$$H(M1) = -\vec{\mu}\cdot\vec{B} = -\mu_z B$$

$$= -\sqrt{\frac{4\pi}{3}}\ M_o(M1)\ B \qquad \text{(A1-24)}$$

If the z-axis is so chosen that its direction is parallel to B, the interaction matrix is

$$\langle Im' \mid H(M1) \mid Im \rangle = \sqrt{\frac{4\pi}{3}}\ B\ \langle Im \mid M_o(M1) \mid Im' \rangle \qquad \text{(A1-25)}$$

when m = m'

$$\langle Im' \mid H(M1) \mid Im \rangle = -\sqrt{\frac{4\pi}{3}}\ B\ \frac{m}{[(2I-1)(I+1)I]^{\frac{1}{2}}}$$

$$\langle I \mid M(M1) \mid I \rangle \qquad \text{(A1-26)}$$

From Eq. A1-23, we obtain

$$E(m) = \langle Im \mid H(M1) \mid Im \rangle$$

$$= -\ g_I\ B\mu_N\ m \qquad \text{(A1-27)}$$

with

$$m = I,\ I-1,\cdots\cdots,\ -I$$

# Appendix II

## Electric Field Gradient

A. The electric field gradient due to 3d-electrons

For a charge e at a distance r from the nucleus, the electric field gradient is

$$eq = \frac{\partial^2}{\partial z^2}\left(-\frac{e}{r}\right)$$

$$= -e\left(\frac{3\cos^2\theta - 1}{r^3}\right) \qquad \text{(A2-1)}$$

where $\theta$ is the angle between the radius vector r and the z-axis (see Fig. A2-1).

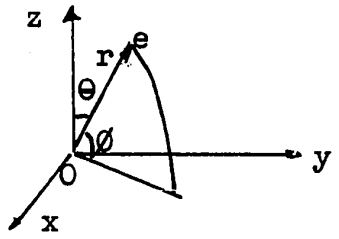


Fig. A2-1 Polar coordinate of a charge e.

When the electron charge is distributed over an orbital, the expectation value is

$$-e\left\langle 3\cos^2\theta - 1\right\rangle \frac{1}{r^3}$$

we can write

$$3\cos^2\theta - 1 = 2\left(\frac{4\pi}{5}\right)^{\frac{1}{2}} Y_2^{\,o} \qquad \text{(A2-2)}$$

and that

$$\langle Y_{\ell}^{m'} \mid Y_L^M \mid Y_{\ell}^{m} \rangle$$
$$= (-1)^{m'} \left[\frac{(2\ell'+1)(2L+1)(2\ell+1)}{4}\right]^{\frac{1}{2}} \begin{pmatrix} \ell' & L & \ell \\ -m' & M & m \end{pmatrix} \times \begin{pmatrix} \ell' & L & \ell \\ 0 & 0 & 0 \end{pmatrix} \qquad \text{(A2-3)}$$

with $-m' + M + m = 0$

Here $Y_L^M$ is an operator, L is the orbital angular quantum number operator, M is the magnetic quantum number operator; $\ell$ and $\ell'$ are theelectron orbital angular quantum numbers; m and m' are the magnetic quantum numbers. $\begin{pmatrix} \ell' & L & \ell \\ -m' & M & m \end{pmatrix}$ is the 3j-symbol. If we consider the d-orbital

$$\langle Y_2^{m'} | Y_2^{o} | Y_2^{m} \rangle = (-1)^{-m'} 5\left(\frac{5}{4\pi}\right)^{\frac{1}{2}} \begin{pmatrix} 2 & 2 & 2 \\ -m' & 0 & m \end{pmatrix} \begin{pmatrix} 2 & 2 & 2 \\ 0 & 0 & 0 \end{pmatrix} \qquad \text{(A2-4)}$$

with the condition $m' = m$

The value of 3j-symbol for different values of m are given in Tab. A2-1.

| m | $\begin{pmatrix} 2 & 2 & 2 \\ -m & 0 & m \end{pmatrix}$ |
|---|---|
| 2 | $2(1/70)^{\frac{1}{2}}$ |
| 1 | $(1/70)^{\frac{1}{2}}$ |
| 0 | $-2(1/70)^{\frac{1}{2}}$ |
| -1 | $(1/70)^{\frac{1}{2}}$ |
| -2 | $2(1/70)^{\frac{1}{2}}$ |

Tab. A2-1 The values of 3j-symbol for $-2 \leq m \leq 2$.

Therefore, we obtain

$$eq \langle r^{-3} \rangle^{-1} = \langle 3 \cos^2 \theta - 1 \rangle \left\langle \frac{1}{r^3} \right\rangle^{-1}$$

$$= \begin{cases} -4/7 & \text{for } d_{z^2} \\ 4/7 & \text{for } d_{x^2 - y^2} \\ -2/7 & \text{for } d_{zx} \\ -2/7 & \text{for } d_{yz} \\ 4/7 & \text{for } d_{xy} \end{cases} \qquad \text{(A2-5)}$$

Similarly

$$eq\eta = \left(\frac{\partial^2}{\partial x^2} - \frac{\partial^2}{\partial y^2}\right)\left(-\frac{e}{r}\right)$$

$$= -e \frac{3 \sin\theta \cos^2\theta - \sin^2\phi}{r^3} \qquad \text{(A2-6)}$$

Also

$$\sin^2\theta (\cos^2\theta - \sin^2\phi) = \sqrt{\frac{8\pi}{5}} \left( Y_2^2 + Y_2^{-2} \right) \qquad \text{(A2-7)}$$

and

$$\left\langle Y_2^m \middle| Y_2^2 + Y_2^{-2} \middle| Y_2^m \right\rangle$$

$$= -10 \left(\frac{5}{4\pi}\right)^{\frac{1}{2}} \left(\frac{1}{70}\right)^{\frac{1}{2}} (-1)^m$$

$$\begin{pmatrix} 2 & 2 & 2 \\ -m' & 2 & m \end{pmatrix} + \begin{pmatrix} 2 & 2 & 2 \\ -m' & -2 & m \end{pmatrix} \qquad \text{(A2-8)}$$

with the conditions,

$m' = 2, \quad 1, \quad 0, \quad -1, \quad -2.$

$m = 0, \quad -1, \quad \pm 2, \quad 1, \quad 0.$

The expectation value of $Y_2^2 + Y_2^{-2}$ vanishes for m or m' equal to ±2 and 0, i.e., for $d_{z^2}$, $d_{x^2-y^2}$ and $d_{xy}$. Using

$$\langle Y_2^1 | Y_2^2 + Y_2^{-2} | Y_2^{-1} \rangle = -(2/7)(15/8)^{\frac{1}{2}} \qquad \text{(A2-9)}$$

in Eq. A2-8, we get

$$q\langle r^{-3}\rangle^{-1} = \begin{cases} 0 \text{ for } d_{z^2} \\ 0 \text{ for } d_{x^2-y^2} \\ 0 \text{ for } d_{xy} \\ 6/7 \text{ for } d_{yz} \\ -6/7 \text{ for } d_{zx} \end{cases} \qquad \text{(A2-10)}$$

q can be reduced from the free ion value by the following factors: (a) the crystal field at finite temperatures, (b) covalency effect. The effect of the crystal field lifts the level of degeneracy. According to Ingalls (ref. 10), the electric field gradient should be multiplied by the covalency parameter $\alpha^2$ and a function

$$F = Z^{-1}\left(1 + \exp -2\Delta_1/kT + \exp -2\Delta_2/kT - \exp -\Delta_1/kT - \exp -\Delta_2/kT - \exp -(\Delta_1+\Delta_2)/kT\right)$$

$$Z = 1 + \exp -\Delta_1/kT + \exp -\Delta_2/kT.$$

where $\Delta_1$ and $\Delta_2$ are the splitting parameters. The function $F(\Delta_1, \Delta_2, T)$ containing the different Boltzman populations of these orbitals account for the variations of the quadrupole splitting at different temperatures.

B. The electric field gradient due to lattice charges

The electric field gradient due to distant point charge $e_i$ are expressed by summing terms of the form of Eq. A2-1 and A2-5. Thus, we have

$$e\,q = \sum_{i=1}^{N} e_i \frac{3\cos^2\theta_i - 1}{r_i^3}$$

$$e\,q\,\eta = \sum_{i=1}^{N} e_i \frac{3\sin\theta_i \cos^2\phi_i}{r_i^3} \qquad \text{(A2-11)}$$

Here $(r_i, \theta_i, \phi_i)$ are the position coordinates of charge $e_i$.

## Appendix III

## Calculation of Electronic Charge Density at Nucleus in Iron Compounds from Experimental Results

For $FeSO_4 \cdot 7H_2O$, the isomer shift with respect to $Na_2Fe(CN)_5 \cdot NO \cdot 2H_2O$ is found to be 0.151 cm/sec as in Tab. IV-1. Substituting this value and the other factors into Eq. IV-1, we have

$$0.151 \text{ cm/sec} = 4.1718 \times 10^{24} \text{ cm}^4/\text{sec} \times (1.8 \times 10^{-3}) \times \left\{ \Psi_a^2(0) - \Psi_{SNP}^2(0) \right\} \text{cm}^{-3} \times 1.32$$

$$\Psi^2_a(0) - \Psi_{SNP}^2(0) = \frac{1.51}{4.1718 \times 10^{-24} \times 1.8 \times 10^{-3} \times 1.32} \text{cm}^{-3} \times 1.48 \times 10^{-25} \text{ cm}^3/a_o^3$$

$$= -2.36 \, a_o^{-3}$$

The factor $1.4820 \times 10^{-25}$ $cm^3/a_o^3$ is for converting the unit of electronic charge density $cm^{-3}$ to $a_o^{-3}$. Since

$$\Psi_{SNP}^2(0) = 11882.80 \, a_o^{-3}$$

therefore,

$$\Psi_a^2(0) = (11882.80 - 2.36) \, a_o^{-3}$$

$$= 11880.54 \, a_o^{-3}$$

# Appendix IV

## Calculation of Electronic Charge Density at Nucleus

The Hamiltonian of Roothaan-Hartree-Fock equation can be written in the form

$$H = \sum_a \left(-\frac{1}{2}\nabla_a^2 - \frac{z}{r_a}\right) + \sum_{a>b} \frac{1}{r_{ab}} \qquad \text{(A4-1)}$$

The total wave function $\Phi$ is in general the sum of several Slater determinants

$$\Phi = \sum_g L_g \phi_g \qquad \text{(A4-2)}$$

$\phi_g$ is an antisymmetrized product of spin-orbitals, which is obtained by solving the Roothaan-Hartree-Fock equation.

The orbitals in each $\phi_g$ are characterized by the indices $\lambda$, $\alpha$ and i, the index $\lambda$, which indicates the symmetry species, corresponds to the quantum number $\ell$; the index $\alpha$, which indicates the subspecies, label the individual members of the degenerate set, that transform according to the representation $\lambda$; and the index i, refers to the ith orbital of symmetry $\lambda$.

The orbital $\phi_{i\lambda\alpha}$ is expanded in terms of basis function according to

$$\phi_{i\lambda\alpha} = \sum_p \chi_{p\lambda\alpha} C_{i\lambda p} \qquad \text{(A4-3)}$$

The subscript p refers to the pth basis function of symmetry $\lambda$. The basis function can be written as

$$\chi_{p\lambda\alpha}(r, \theta, \phi) = R_{\lambda p}(r)\, Y_\lambda^\alpha(\theta, \phi) \qquad \text{(A4-4)}$$

where

$$R_{\lambda p} = \left[(2n_{\lambda p})!\right]^{\frac{1}{2}} (2\zeta_{\lambda p})^{n_{\lambda p}+\frac{1}{2}} r^{n_{\lambda p}-1} e^{\zeta_{\lambda p} r} \qquad \text{(A4-5)}$$

and $Y_{\lambda}^{\alpha}(\theta, \phi)$ are normalized spherical harmonics.

Since only the s-electrons have the contribution of charge density at nucleus, we consider the wave function of $n_{\lambda p} = \lambda + 1 = 0$ only. The wave function for the s-orbital thus becomes

$$\varphi_i = \sqrt{\frac{1}{4\pi}} \cdot 2 \left\{ \left( C_{i1} \zeta_1^{3/2} + C_{i2} \zeta_2^{3/2} \right) \right\} \qquad \text{(A4-6)}$$

For iron, i has the value from 1 to 4 corresponding to 1s, 2s, 3s and 4s orbital.

The values of the parameters are given in "Tables of Atomic Functions" by Enrico Clement. For iron of $^5D$ state, the basis functions and the parameters are given as (ref. 16)

$\zeta_1 = 25.87820$ $\qquad$ $\zeta_2 = 38.73300$

$C_{11} = 0.95050$ $\qquad$ $C_{12} = 0.02057$

$C_{21} = -0.31119$ $\qquad$ $C_{22} = 0.00637$

$C_{31} = 0.11608$ $\qquad$ $C_{32} = -0.00282$

$C_{41} = -0.02450$ $\qquad$ $C_{42} = 0.00041$

Substuting these values into Eq. A4-6, the wave function of an electron corresponding to each s-orbital is obtained,

$$\varphi_1 = 73.39$$
$$\varphi_2 = -22.24$$
$$\varphi_3 = 8.23$$
$$\varphi_4 = -1.76$$

The electronic charge density of each electron at nucleus is then the square of the wave function, therefore (ref. 17, 18, 19, 20, 21, 22, 23),

$$\rho_1 = 5386.36$$
$$\rho_2 = 494.50$$
$$\rho_3 = 67.86$$
$$\rho_4 = 3.11$$

in $a_o^{-3}$.

There are two electrons in each of 1s, 2s and 3s orbital and 4s-electron percentage contribution of each compound is given in Tab. IV-3. The electronic charge density at nucleus is then equal to

$$2\rho_1 + 2\rho_2 + 2\rho_3 + X\rho_4$$

X being the 4s-electron percentage contribution.

For $FeCl_2 \cdot 4H_2O$, X is found to be 1.5 %, therefore, the electronic charge density is

$$2 \times (5382.56 + 494.50 + 67.86) + 3.11 \times 1.5\ \%$$
$$= 11898.69$$

in $a_o^{-3}$.

# Appendix V

## Mössbauer Effect Spectra for Different Iron Compounds

Fig. A5-1 through A5-8 give the corrected Mössbauer Effect spectra observed in our experiments.

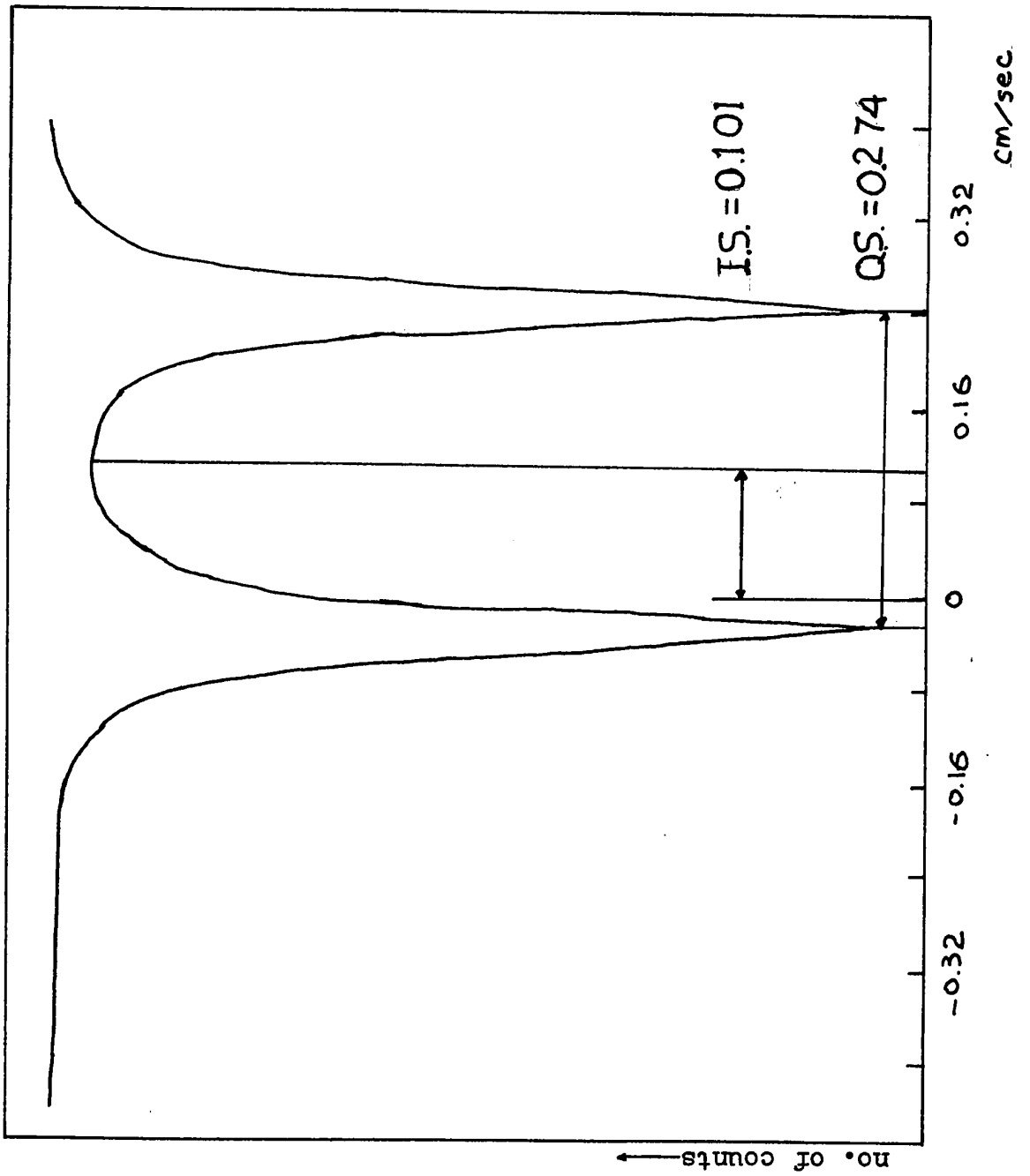


Fig. A5-1 The Mössbauer Effect spectrum of $FeSO_4 \cdot 7H_2O$ at room temperature.

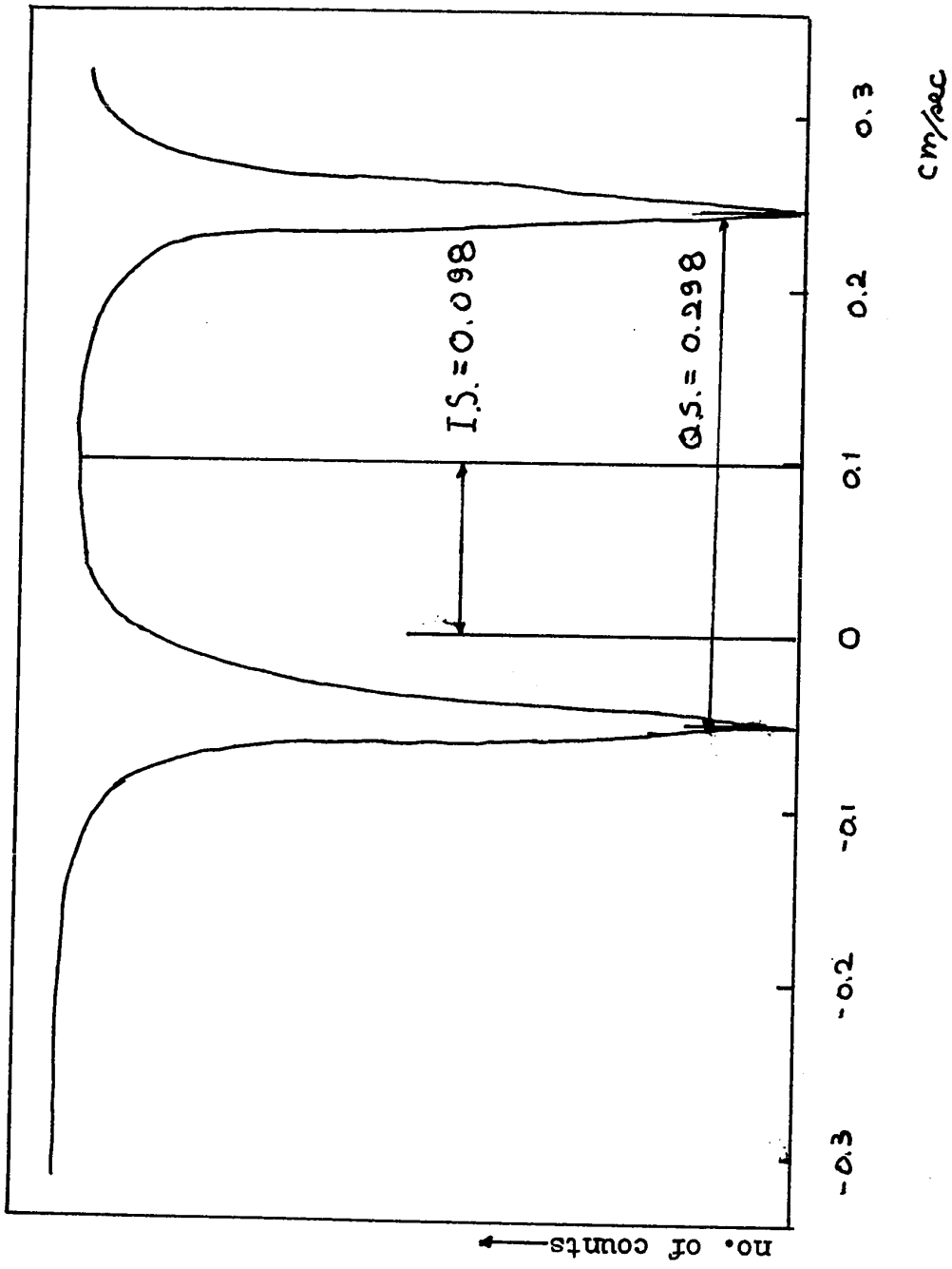


Fig. A5-2 The Mössbauer Effect spectrum of $FeCl_2 \cdot 4H_2O$ at room temperature.

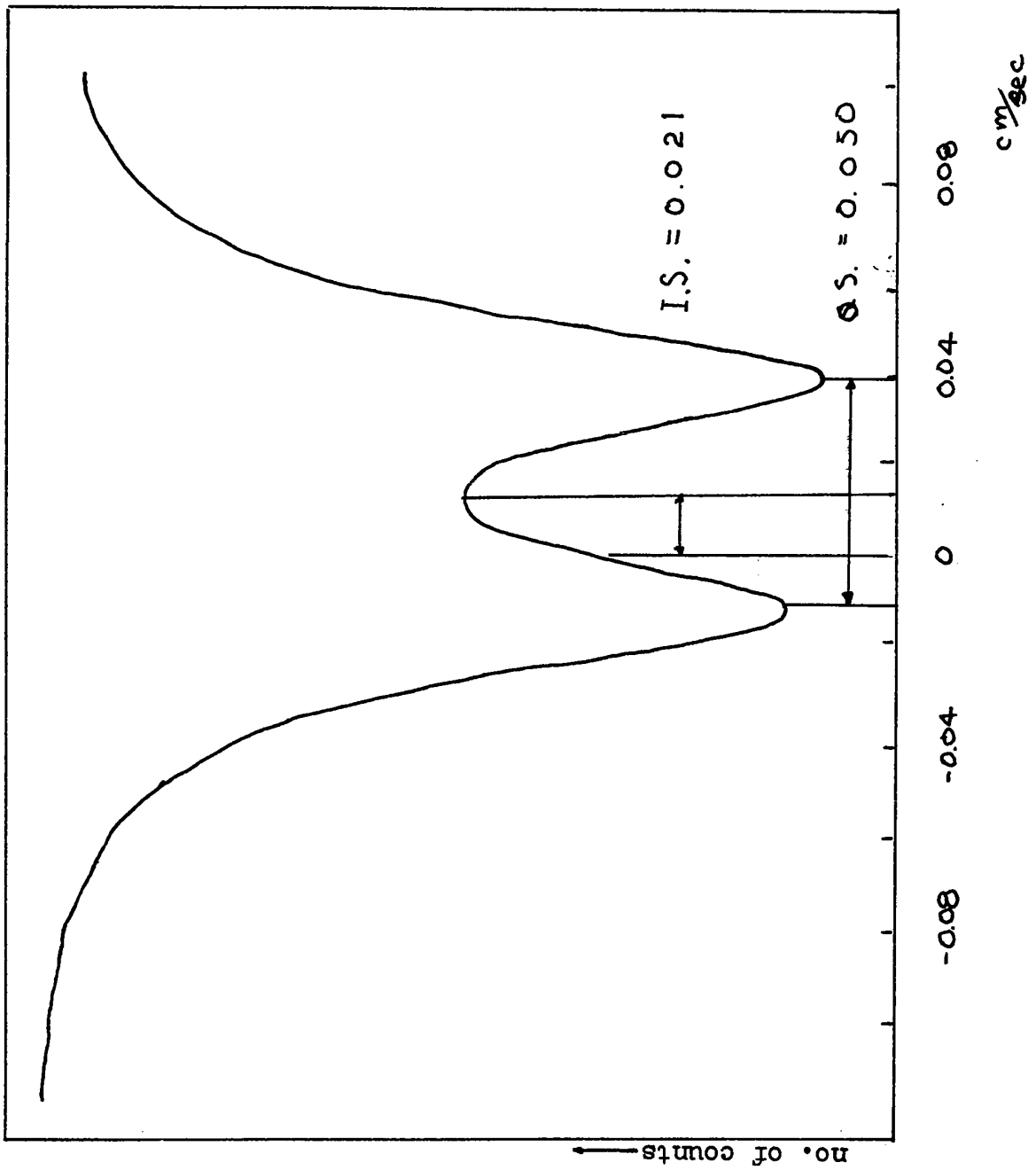


Fig. A5-3 The Mössbauer Effect spectrum of $Fe(SO_4)_3 \cdot 9H_2O$ at room temperature.

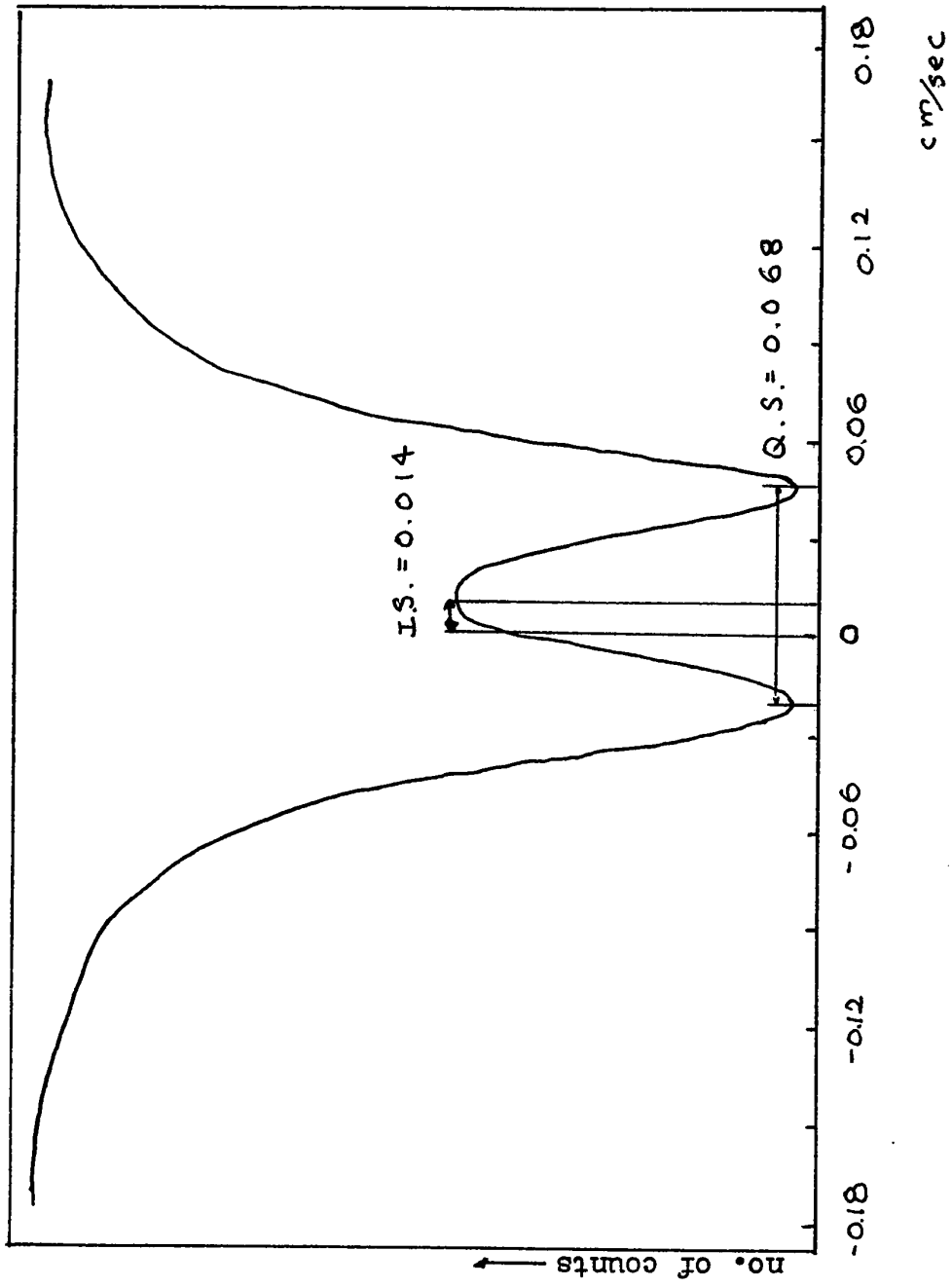


Fig. A5-4 The Mössbauer Effect spectrum of $FeCl_3 \cdot 6H_2O$ at room temperature

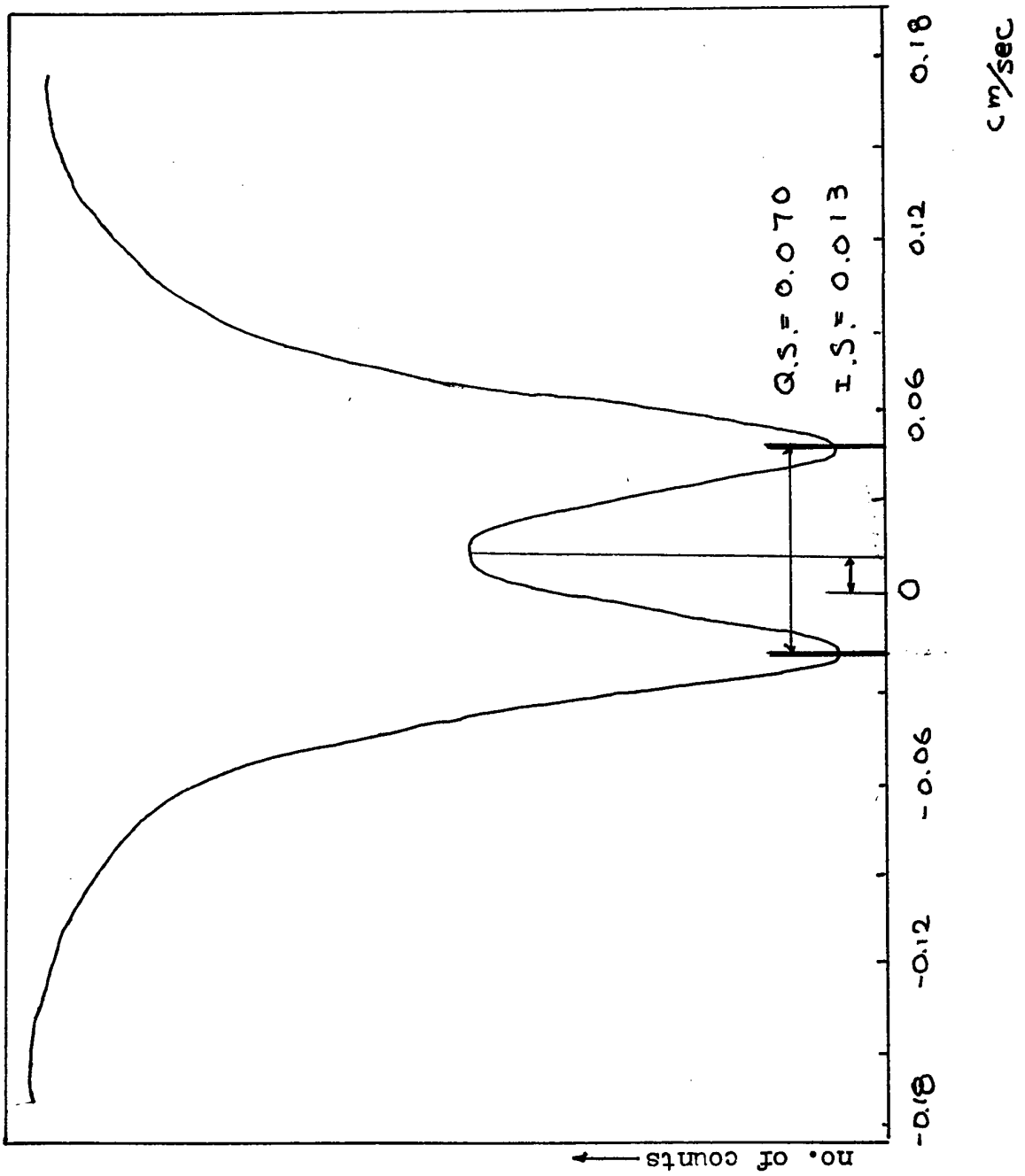


Fig. A5-5 The Mössbauer Effect spectrum of $Fe(NO_3)_3 \cdot 9H_2O$ at room temperature.

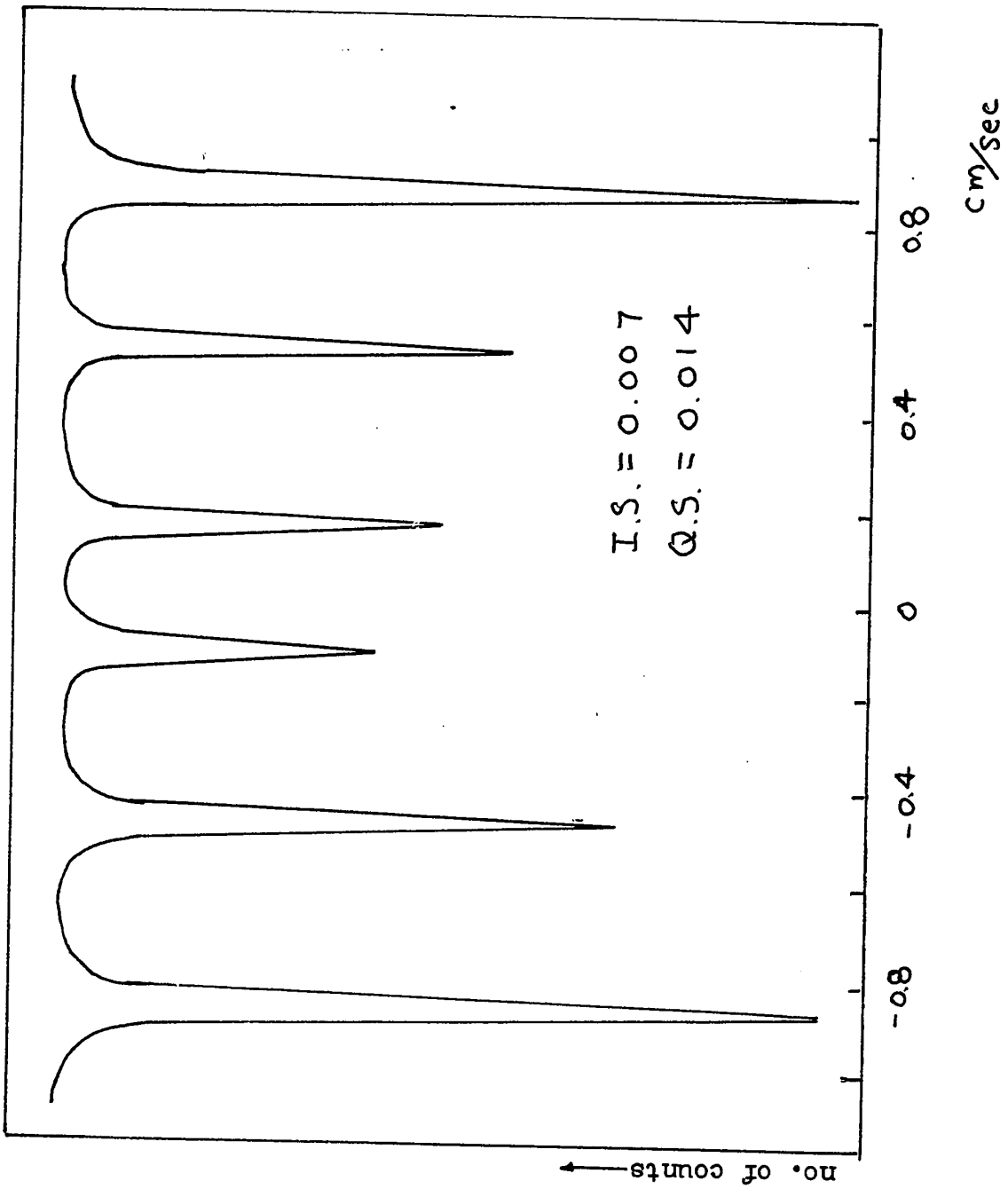


Fig. A5-6 The Mössbauer Effect spectrum of $Fe_2O_3$ at room temperature.

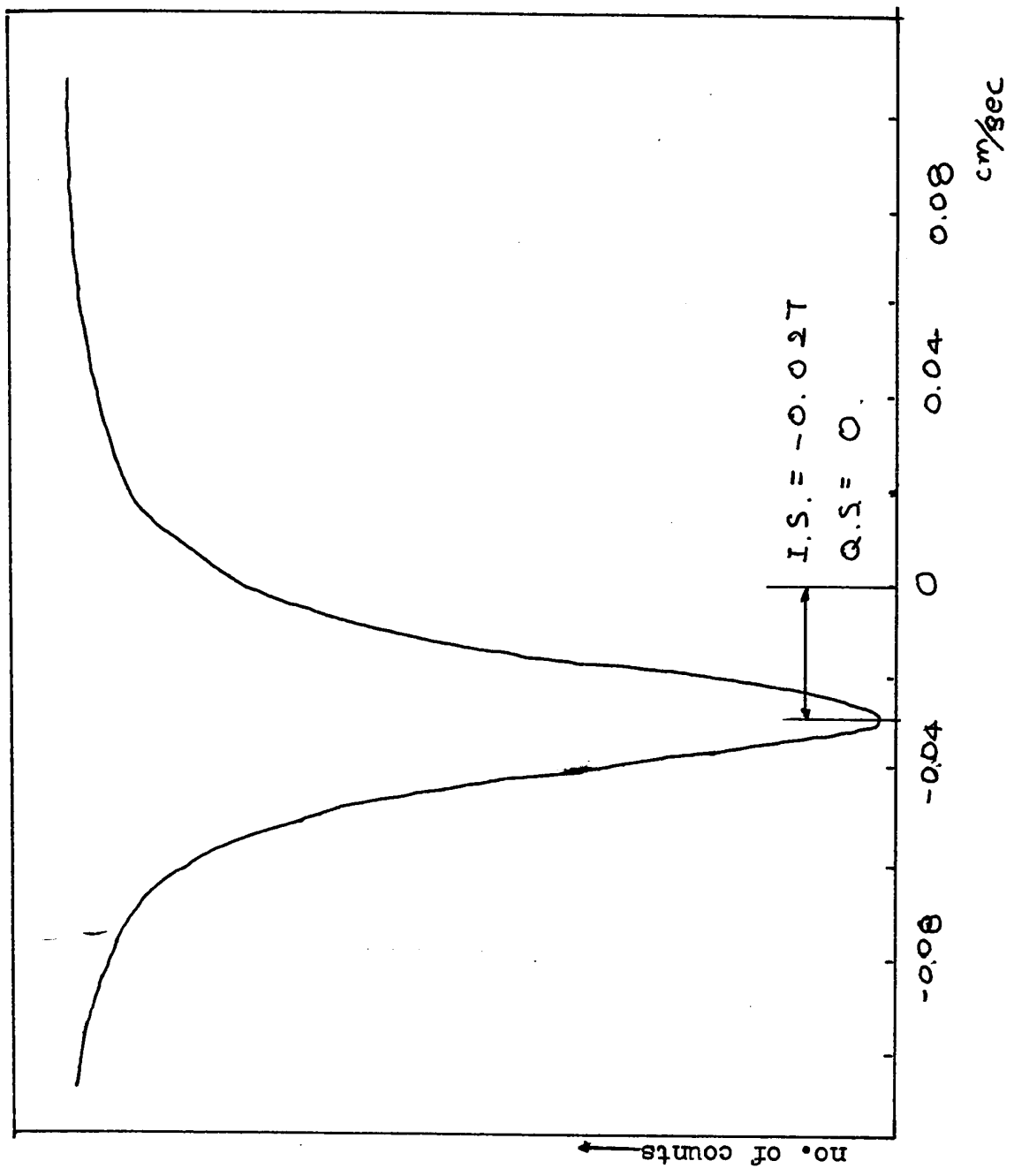


Fig. A5-7 The Mössbauer Effect spectrum of $K_4Fe(CN)_6 \cdot 3H_2O$ at room temperature.

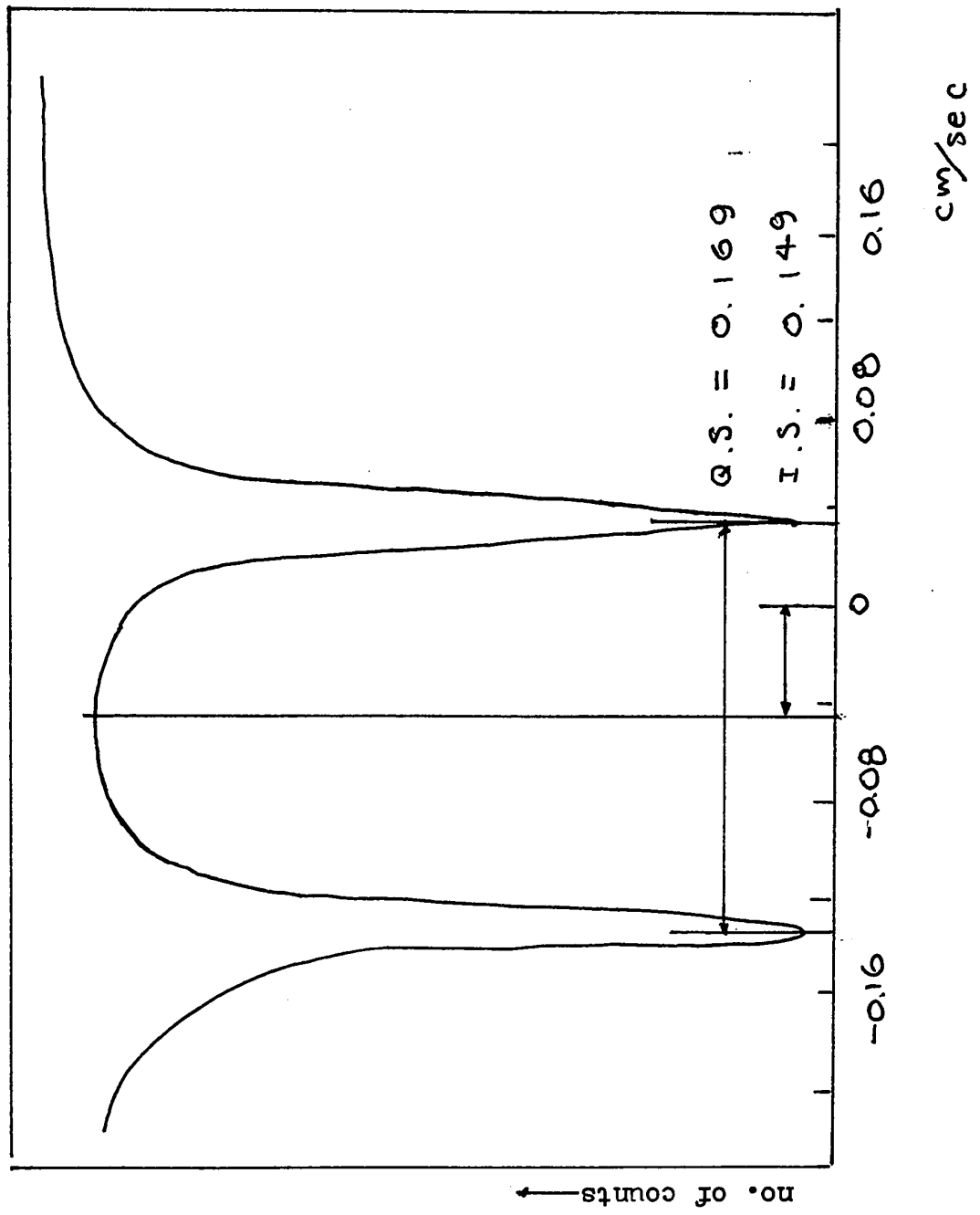


Fig. A5-8 The Mössbauer Effect spectrum of $Na_2Fe(CN)_5NO \cdot 2H_2O$ at room temperature.

# References


1. W. Kuhn, Phil. Mag. 8, 625 (1929)
2. G. Ludwig, Z. Phys. 130, 468 (1951)
3. R. L. Mössbauer, Z. Phys. 124 (1958)
4. P. B. Moon, Proc. Phys. Soc. 63, 1189 (1950)
5. F. L. Shapiro, Soviet Phys. Up. 4, 881 (1961)
6. L. R. Walker, G. K. Wertheim and V. Jaccarino, Phys. Rev. Letters 6, 60 (1961)
7. J. J. Spijkerman, F. C. Ruegg and L. May, "Mössbauer Effect Methodology" Vol. 2, p85, Plenum Press, New York
8. The Mössbauer Effect and Its Application in Chemistry, Advanced in Chemistry Series 68, American Society 1967, p55
9. O. C. Kistner and A. W. Sunyar, Phys. Rev. Letters, 4, 412 (1960)
10. R. Ingalls, Phys. Rev. 133, A 787
11. H. M. Foley, R. M. Sternheimer and G. Tycko, Phys. Rev. 102, 731 (1956)
12. H. M. Foley, R. M. Sternheimer and G. Tycko, Phys. Rev. 93, 734 (1954)
13. H. M. Foley, R. M. Sternheimer and G. Tycko, Phys. Rev. 84, 244 (1951)
14. Hans Frauenfelder, "The Mössbauer Effect", W. A. Benjamin, Inc. New York, 1962

15. G. K. Wertheim "Mössbauer Effect: Principles and Applications", Academic Press, New York and London, 1964

16. D. A. Shirley, Rev. Mod. Phys. Vol. 36, No. 1, 342, 1964

17. D. A. Shirley, Rev. Mod. Phys. Vol. 36, No. 1, 343 1964

18. Enrico Clementi, Tables of Atomic Functions 1965 IBM

19. Enrico Clementi, IBM Journal 9, 2 (1965)

20. C. C. J. Roothaan, Rev. Mod. Phys. 23, 69 (1951)

21. C. C. J. Roothaan, Rev. Mod. Phys. 32, 179 (1951)

22. C. C. J. Roothaan and P. Bagus, Methods in Computational Physics, Vol.2, Academic Press, Inc. New York, 1960

23. D. R. Hartree, The calculation of Atomic Structures, John Wiley and Sons, New York, 1957

24. J. S. Slater, Quantum Theory of Atomic Structures, Vols. 1 and 2, McGraw-Hill Book Company, Inc., New York, 1960

25. G. K. Wertheim, J. Appl. Phys. Suppl. 32, No. 3, 110S (1961)